Numerical modeling of senile plaque development under conditions of limited diffusivity of amyloid-β monomers

Andrey V. Kuznetsov

Department of Mechanical and Aerospace Engineering, North Carolina State University,

Raleigh, NC 27695-7910, USA; e-mail: avkuznet@ncsu.edu

Abstract

This paper introduces a method to simulate the progression of senile plaques, focusing on scenarios where concentrations of amyloid beta (Aβ) monomers and aggregates vary between neurons. Extracellular variations in these concentrations may arise from the limited diffusivity of Aβ monomers and a high rate of Aβ monomer production at lipid membranes, requiring a substantial concentration gradient for diffusion-driven transport of Aβ monomers. The dimensionless formulation of the model is presented, highlighting four key dimensionless parameters governing the solutions for Aβ monomer and aggregate concentrations, as well as the radius of a growing Aβ plaque within the control volume. These parameters include the dimensionless diffusivity of Aβ monomers, the dimensionless rate of Aβ monomer production, and the dimensionless half-lives of Aβ monomers and aggregates. An approximate solution is derived for the scenario involving large diffusivity of Aβ monomers and dysfunctional protein degradation machinery, resulting in infinitely long half-lives for Aβ monomers and aggregates. In this scenario, the concentrations of Aβ aggregates and the radius of the Aβ plaque depend solely on a single dimensionless parameter that characterizes the rate of Aβ monomer production. According to the approximate solution, the concentration of Aβ aggregates is linearly dependent on the rate of monomer production, and the radius of an Aβ plaque is directly proportional to the cube root of the rate of monomer production. However, when departing from the conditions of the approximate solution (e.g., finite half-lives), the concentrations of Aβ monomers and aggregates, along with the plaque radius, exhibit complex dependencies on all four dimensionless parameters. For instance, under physiological half-life conditions, the plaque radius reaches a maximum value and stabilizes thereafter.

Keywords: neuron; Alzheimer's disease; Finke−Watzky model, mathematical modeling; neurotoxicity; neurodegenerative disease

Abbreviations

Aβ	amyloid beta
AD	Alzheimer's disease
APP	amyloid precursor protein
CV	control volume
F-W	Finke-Watzky
PDE	partial differential equation

1. Introduction

Modeling the progression of amyloid-beta (Aβ) plaques poses a significant challenge in the field of mathematical biology, driven by their crucial role as a hallmark of Alzheimer's disease (AD). AD is a severe neurodegenerative disorder that leads to dementia, impacting over 30 million individuals globally [1-4]. Characterized by the presence of Aβ plaques and neurofibrillary tangles containing the tau protein [5,6], AD's exact relationship with Aβ plaques remains uncertain. These plaques might act as causative agents, benign markers, or even protective factors in the disease [7-10]. Despite this ambiguity, the gradual accumulation of Aβ plaques precedes irreversible neurodegeneration [11]. A comprehensive understanding of the temporal dynamics of Aβ plaque growth is crucial for the early diagnosis and treatment of AD [12].

The formation of an Aβ plaque is a complex process that encompasses the production of Aβ monomers, their transport within the cytosol driven by diffusion, their transformation into Aβ aggregates through nucleation and autocatalytic mechanisms, the degradation of monomers and aggregates via proteolytic processes, and the assembly of Aβ aggregates into a cohesive Aβ plaque.

Aβ monomers result from the cleavage of amyloid precursor protein (APP) by β- and γ-secretases [8,13,14]. Following their release into the extracellular environment, Aβ monomers undergo diffusion in the cytosol [15,16]. Extracellular Aβ monomers possess the potential to aggregate [17]. The aggregation of Aβ monomers was modeled using the Finke-Watzky (F-W) model [18,19]. It was assumed that all Aβ aggregates become part of Aβ plaques, and the process of plaque formation from aggregates was considered sufficiently fast, making it a non-limiting stage in the model. The proteolytic degradation of Aβ monomers and aggregates was simulated by assuming finite half-lives for these components.

This paper aims to expand upon my previous investigations into the effect of Aβ monomer diffusivity [20] and studies based on the lumped capacitance approximation of Aβ plaque growth [21]. The objective is to develop a method for predicting the growth of Aβ plaques in scenarios where the concentrations of Aβ monomers and aggregates vary across the control volume (CV), thereby not adhering to the lumped capacitance assumption. The model enables the analysis of factors such as Aβ monomer production, diffusion-driven transport of Aβ monomers, the kinetic rate of conversion of Aβ monomers into aggregates, and the half-lives of Aβ monomers and aggregates due to proteolytic degradation. The model is presented in a dimensionless form to minimize the number of parameters influencing the model's solution. The impact of each dimensionless parameter on the concentrations of Aβ monomers and aggregates, as well as the radius of the Aβ plaque, is examined.

2. Materials and models

2.1. Model equations

The F-W model is employed to simulate the conversion of Aβ monomers into aggregates. This conversion takes place through two mechanisms: nucleation and autocatalysis. During the nucleation step, new aggregates are continuously formed (as described in Eq. (1) below), and in the autocatalysis step, there is rapid surface growth of these aggregates (as described in Eq. (2) below) [18,19]:

$$A \xrightarrow{k_1} B\,, \tag{1}$$

$$A + B \xrightarrow{k_2} 2B\,, \tag{2}$$

where A represents a monomeric protein, and B represents an amyloid-converted protein. The kinetic constants, k_1 and k_2, represent the rates of nucleation and autocatalytic growth, respectively [18]. Eqs. (1) and (2) describe pseudo-elementary reactions, which, in reality, involve a much larger number of reaction steps.

The typical application of the F-W model involves the situation when a given initial concentration of monomers is converted into aggregates [19]. In this paper, the model is applied to a situation where monomers are continuously supplied to the control volume (CV) through a boundary located at x=0 (see Fig. 1). The generation of monomers occurs through the cleavage of APP by β- and γ-secretases at lipid membranes, such as a cellular membrane [8,14,22,23].

Expressing the conservation of Aβ monomers yields:

$$\frac{\partial C_A}{\partial t} = D_A \frac{\partial^2 C_A}{\partial x^2} - k_1 C_A - k_2 C_A C_B - C_A \frac{\ln(2)}{T_{1/2,A}}\,. \tag{3}$$

Expressing the conservation of Aβ aggregates yields:

$$\frac{\partial C_B}{\partial t} = k_1 C_A + k_2 C_A C_B - C_B \frac{\ln(2)}{T_{1/2,B}}\,. \tag{4}$$

The initial conditions are described by the following equations:

$$\text{At } t = 0\text{: } C_A = 0\,,\ C_B = 0\,. \tag{5a,b}$$

The boundary conditions are expressed through the following equations:

At $x = 0$: $-D_A \frac{\partial C_A}{\partial x} = q_{A,0}$, (6)

At $x = L$: $\frac{\partial C_A}{\partial x} = 0$. (7)

Eq. (6) posits that Aβ monomers are released from the boundary located at x=0. The boundary at x=L is modeled as a symmetric one. The model employs the independent variables listed in Table 1, while Table 2 outlines the dependent variables. Table 3 gives a summary of the parameters used in the model.

Table 1. Independent variables employed in the model.

Symbol	Definition	Units
t	Time	s
x	Linear coordinate measuring the distance from the surface of the control volume through which Aβ monomers are supplied	μm

Table 2. Dependent variables used in the model.

Symbol	Definition	Units
C_A	Molar concentration of Aβ monomers	μM
C_B	Molar concentration of Aβ aggregates	μM

Table 3. Parameters utilized in the model.

Symbol	Definition	Units	Value or range	Reference or estimation method	Value(s) used in computations
a_{21}	Conversion factor from $\frac{\text{mol}}{\mu\text{m}^3}$ to μM	$\frac{\mu\text{M}\ \mu\text{m}^3}{\text{mol}}$	10^{21}		10^{21}

$C_{A,0}$	Concentration of Aβ monomers	μM	0.25×10^{-3} - 0.425×10^{-3} [a]	[15]	
$C_{B,tox}$	Neurotoxic concentration of Aβ oligomers	μM	50 [b] (corresponds to $C_B^* = 2.13\times10^5$)	[24]	
D_A	Diffusivity of Aβ monomers	$\mu m^2/s$	62.3 [c]	[15]	62.3
k_1	Rate constant for the first pseudo-elementary step of the F-W model, describing the nucleation of Aβ aggregates	s^{-1}	2.22×10^{-9} [d]	[18,25]	2.22×10^{-9}
k_2	Rate constant for the second pseudo-elementary step of the F-W model, describing the autocatalytic growth of Aβ aggregates	$\mu M^{-1}\ s^{-1}$	9.44×10^{-6} [d]	[18,25]	9.44×10^{-6}
L	Half distance between senile plaques	μm	50	Estimated from Fig. 1a in [26]	50
MW	Molecular weight of an Aβ monomer, defined as the sum of	$g\ mol^{-1}$	4.51×10^3 [e]	[24]	4.51×10^3

	the weights of every atom in the monomer				
$q_{A,0}$	Flux of Aβ monomers from the left-hand side boundary of the CV with a volume L^3	μM μm s^{-1}	1.1×10^{-5} [f]	[24]	1.1×10^{-5}
t_f	Duration of time during which senile plaques grow	s	3.15×10^{8} [g]	[27]	3.15×10^{8}
$T_{1/2,A}$	Half-life of Aβ monomers	s	4.61×10^{3} [h]	[15]	4.61×10^{3}, 10^{20} (to represent $T_{1/2,A}\to\infty$)
$T_{1/2,B}$	Half-life of Aβ aggregates	s	2.31×10^{4} [i]		2.31×10^{4}, 10^{20} (to represent $T_{1/2,B}\to\infty$)
ρ	Density of the Aβ plaque	g/μm^3	1.35×10^{-12} [j]	[28]	1.35×10^{-12}

[a] The parameter ranges from 250 pM to 425 pM, as reported in [15]. While this parameter is not directly involved in the model, it is included in the table as it contributes to the discussion on the predicted concentration of Aβ monomers by the model.

[b] The value corresponds to the Aβ42 isoform [24]. Although this parameter is not directly utilized in the model, it is included in the table because it is pertinent to the discussion of the model's predictions concerning the time it takes for Aβ aggregates to reach the neurotoxic concentration.

[c] The diffusivity value is 0.623×10^{-6} cm^2/s [15]. This value is smaller than the one reported in [16] (1.43×10^{-6} cm^2/s) because the estimate provided in [15] considers the effect of tortuosity. Tortuosity factors in the reduction of diffusion in brain tissue caused by various barriers, such as cells and the extracellular matrix.

[d] Values reported in [18] were obtained by curve-fitting data from [25]. $k_1 = 8\times10^{-6}$ h^{-1}, $k_2 = 3.4\times10^{-2}$ μM^{-1} h^{-1} [18].

[e] Molecular weight of Aβ42 [24].

[f] As per [24], the human brain generates Aβ42 monomers at a rate of 0.33×10^{-6} μmol s^{-1}. Taking into account the approximate brain volume of 1.5×10^{15} μm^3, the production rate of Aβ42 per unit volume is estimated to be 2.2×10^{-22} μmol μm^{-3} s^{-1}. In a small cube with a side length of L (representing the CV in Fig. 1), the Aβ42 production rate is 2.75×10^{-17} μmol s^{-1}. The production of Aβ monomers takes place at the lipid membrane [29]. Assuming that all Aβ42 is released from the left-hand side face of the cube with an area of L^2, the release rate of Aβ42 per unit area is 1.1×10^{-20} μmol μm^{-2} s^{-1} $=1.1\times10^{-5}$ μM μm s^{-1}.

[g] A duration of 10 years was employed as an estimate for the growth of a senile plaque [27].

[h] As per [15], the value is 1.28 hours.

[i] Aβ aggregates have a longer half-life compared to monomers [30,31]. This study assumes that the half-life of Aβ aggregates is five times longer than that of monomers.

[j] A commonly employed density value, irrespective of the protein type, is 1.35 g/cm³ [28].

2.2. Dimensionless model equations

The dimensionless independent variables employed in the model are summarized in Table 4, while the dimensionless dependent variables are given in Table 5. A summary of the dimensionless parameters utilized in the model is provided in Table 6.

The model, expressed by Eqs. (3)-(7), is reformulated in its dimensionless form as follows:

$$\frac{\partial C_A^*}{\partial t^*} = D_A^* \frac{\partial^2 C_A^*}{\partial x^{*2}} - C_A^* - C_A^* C_B^* - C_A^* \frac{\ln(2)}{T_{1/2,A}^*}, \tag{8}$$

$$\frac{\partial C_B^*}{\partial t^*} = C_A^* + C_A^* C_B^* - C_B^* \frac{\ln(2)}{T_{1/2,B}^*}, \tag{9}$$

At $t^* = 0$: $C_A^* = 0$, $C_B^* = 0$, (10a,b)

At $x^* = 0$: $-D_A^* \frac{\partial C_A^*}{\partial x^*} = q_{A,0}^*$, (11)

At $x^* = 1$: $\frac{\partial C_A^*}{\partial x^*} = 0$. (12)

To explore the effect of different model parameters, Eqs. (8)-(12) are solved numerically. The numerical solution is then compared with the approximate solution of Eqs. (8)-(12) obtained in [21]. The approximate solution, detailed in section S1 of the Supplemental Materials, is derived under the assumption of dysfunctional protein degradation machinery, implying infinitely large half-lives for Aβ monomers and aggregates ($T_{1/2,A}^* \to \infty$ and $T_{1/2,B}^* \to \infty$).

Table 4. Dimensionless independent variables employed in the model.

Symbol	Definition
t^*	$t k_1$
x^*	x / L

Table 5. Dimensionless dependent variables utilized in the model.

Symbol	Definition
C_A^*	$C_A k_2 / k_1$
C_B^*	$C_B k_2 / k_1$
r_{ABP}^*	r_{ABP} / L

Table 6. Dimensionless parameters utilized in the model.

Symbol	Definition	Value(s) obtained using the dimensional parameter values listed in the final column of Table 3
D_A^*	$D_A / \left(L^2 k_1\right)$	1.12×10^7

$q_{A,0}^*$	$q_{A,0}k_2/\left(k_1^2 L\right)$	4.21×10^5
t_f^*	$t_f k_1$	0.700
$T_{1/2,A}^*$	$T_{1/2,A}k_1$	1.02×10^{-5}, 2.22×10^{11} (to represent $T_{1/2,A}^*\to\infty$)
$T_{1/2,B}^*$	$T_{1/2,B}k_1$	5.12×10^{-5}, 2.22×10^{11} (to represent $T_{1/2,B}^*\to\infty$)
ρ^*	$\frac{\rho}{MW}a_{21}\frac{k_2}{k_1}$	1.27×10^9

The model developed in this paper does not simulate the process in which adhesive Aβ fibrils come together to form an Aβ plaque. It is presumed that this assembly process happens more rapidly than the creation of Aβ fibrils.

The growth of the Aβ plaque (Fig. 1) is simulated employing the following method. The total count of Aβ monomers integrated into the Aβ plaque, represented as *N*, at a given time *t*, is calculated using the following equation [32]:

$$N(t)=\frac{L^2 N_A}{a_{21}}\left(2\int_0^L C_B(t)\,dx\right). \tag{13}$$

The factor of 2 preceding the integral in Eq. (13) is employed because the model posits that the Aβ plaque forms between two neurons, with each membrane releasing Aβ monomers at a rate of $q_{A,0}$ (Fig. 1).

Alternatively, $N(t)$ can be calculated as outlined in [32]:

$$N(t)=\frac{V_{ABP}(t)\rho}{MW}N_A, \tag{14}$$

where MW denotes the average molecular weight of an Aβ monomer.

By setting the expressions on the right-hand sides of Eqs. (13) and (14) equal and solving for the volume of an Aβ plaque, the following result is obtained:

$$V_{ABP}(t) = \frac{L^2}{a_{21}} \frac{MW}{\rho} \left(2\int_0^L C_B(t)\,dx \right), \tag{15}$$

where $a_{21} = 10^{21} \frac{\mu\text{M}\ \mu\text{m}^3}{\text{mol}}$ denotes the conversion factor from $\frac{\text{mol}}{\mu\text{m}^3}$ to μM.

Assuming that the Aβ plaque is spherical in shape,

$$V_{ABP}(t) = \frac{4}{3}\pi r_{ABP}^3(t). \tag{16}$$

Setting the right-hand sides of Eqs. (15) and (16) equal and solving for the radius of the Aβ plaque, the following result is obtained:

$$r_{ABP} = \left(\frac{3}{4\pi} \frac{L^2}{a_{21}} \frac{MW}{\rho} \left(2\int_0^L C_B(t)\,dx \right) \right)^{1/3}. \tag{17}$$

Expressed in dimensionless variables, Eq. (17) becomes:

$$r_{ABP}^* = \left(\frac{3}{4\pi} \frac{1}{\rho^*} \left(2\int_0^1 C_B^*(t^*)\,dx^* \right) \right)^{1/3}. \tag{18}$$

If an approximate solution for C_B^* given by Eq. (S10) is used in Eq. (18), the following approximate solution for r_{ABP}^* is obtained:

$$r_{ABP,appr}^* = \left(\frac{3}{4\pi} \frac{(2q_{A,0}^*)}{\rho^*} \right)^{1/3} (t^*)^{1/3}. \tag{19}$$

Returning to the dimensional variables, Eq. (19) can be reformulated as:

$$r_{ABP,appr} = \left(\frac{3}{2\pi} q_{A,0} \frac{MW}{\rho a_{21}} L^2 \right)^{1/3} t^{1/3}. \tag{20}$$

Eq. (20) suggests that the radius of an Aβ plaque is directly proportional to the cube root of the plaque's growth time. This equation indicates that, at large times, the plaque growth is restricted by Aβ peptide production, $q_{A,0}$, and is independent of kinetic constants, k_1 and k_2. This aligns with the results reported in [33] for the late stage of plaque growth, referred to in [33] as the late asymptotic phase. It should be noted that Eq. (20) (Eq. (19) in the dimensionless form) applies only to the situation when the protein

degradation machinery is dysfunctional, and half-lives of Aβ monomers and aggregates are infinitely long, while Eq. (18) applies for any half-life of Aβ monomers and aggregates. In various figures, the predictions obtained from Eq. (18) are compared with predictions that follow from the approximate analytical solution (19).

Eq. (19) is valid for large times. To investigate how the radius of the Aβ plaque increases when $t^* \to 0$, Eq. (S9) is substituted into Eq. (18). This gives the following result for the initial growth of the plaque:

$$r_{ABP}^* = \left(\frac{3}{4\pi} \frac{q_{A,0}^*}{\rho^*} \right)^{1/3} \left(t^* \right)^{2/3}. \tag{21}$$

Returning to dimensional variables, Eq. (21) can be reformulated as:

$$r_{ABP} = \left(\frac{3}{4\pi} q_{A,0} k_1 \frac{MW}{\rho a_{21}} L^2 \right)^{1/3} t^{2/3}. \tag{22}$$

Eq. (22) indicates that during the initial growth of the plaque, its radius is influenced by the rate of nucleation of Aβ aggregates, k_1.

2.3. Numerical solution

Eqs. (3) and (4) constitute a system of two partial differential equations (PDEs). They were solved with initial conditions given by Eq. (5) and boundary conditions given by Eqs. (6) and (7), using MATLAB's PDEPE solver (MATLAB R2020b, MathWorks, Natick, MA, USA). A (100,100) solution mesh was employed, except for Fig. S12, where a (1000,1000) solution mesh was used. In addition to the boundary conditions on C_A^*, PDEPE requires boundary conditions on C_B^* at both ends of the domain. Since Aβ aggregates are assumed to have zero diffusivity (as per Eq. (4)), zero boundary conditions on the diffusion flux of C_B^* are imposed on both sides of the domain. Numerical integration of C_B^* with respect to x^* in Eq. (18) was conducted using MATLAB's TRAPZ solver, implementing the trapezoidal method.

3. Results

3.1. Dimensionless parameters

In this study, the effects of four dimensionless parameters were explored: (1) dimensionless diffusivity of Aβ monomers, $D_A^* = D_A / \left(L^2 k_1\right)$; (2) dimensionless rate at which Aβ monomers are produced, $q_{A,0}^* = q_{A,0} k_2 / \left(k_1^2 L\right)$; (3) dimensionless half-life of Aβ monomers, $T_{1/2,A}^* = T_{1/2,A} k_1$; (4) dimensionless half-life of Aβ aggregates, $T_{1/2,B}^* = T_{1/2,B} k_1$. The other two parameters from Table 6 were kept constant at the following values: $t_f^* = 0.700$ (equivalent to $t_f = 10$ years) and $\rho^* = 1.27 \times 10^9$ (equivalent to 1.35 g/cm³).

3.2. Effects of variating the dimensionless diffusivity

Effects of varying the dimensionless diffusivity of Aβ monomers, D_A^*, are analyzed in Figs. 2, 3, and Figs. S1-S3 in the Supplemental Materials.

The dimensionless concentrations of Aβ monomers and aggregates, C_A^* and C_B^*, respectively, increase with the increase in D_A^*, until D_A^* reaches a value of 10^6 (corresponding to D_A of approximately 5 μm²/s for the values of L and k_1 given in Table 3). It is worth noting that 5 μm²/s is an order of magnitude lower than the physiological value of 62.3 μm²/s given in Table 3. For values of D_A^* greater than this threshold, C_A^* and C_B^* stabilize at a constant level, indicating that beyond this point, they are no longer constrained by diffusion (Fig. 2). In the scenario of dysfunctional protein degradation in neurons, with infinite half-lives for Aβ monomers and aggregates, the neurotoxic concentration of 50 μM (refer to Table 3) is reached when D_A^* exceeds 10^5, equivalent to D_A of around 0.5 μm²/s (which is two orders of magnitude less than the physiological value of 62.3 μm²/s). The approximate solutions for C_A^* and C_B^* (given by Eqs. (S11) and (S10), respectively) do not depend on D_A^*. This is because the approximate solution is obtained under the lumped capacitance assumption, which assumes that C_A^* and C_B^* are independent of x^* but only depend on time t^*. This corresponds to the assumption that $D_A^* \to \infty$. For this reason, the numerical solution computed for the scenario $T_{1/2,A}^* \to \infty$ and $T_{1/2,B}^* \to \infty$ (the scenario for which the approximate solution was obtained) approaches the approximate solution for $D_A^* > 10^7$ (Fig. 2).

A reduction in the dimensionless diffusivity, D_A^*, amplifies variations in C_A^* and C_B^* across the control volume (CV) (Fig. S1). The numerical solution for a large value of D_A^* (1.12×10^8) almost aligns with the approximate solution, represented by a horizontal line, as the approximate solution is unaffected by x^*.

The decrease in D_A^* has minimal effect on C_A^* at the right-hand side boundary of the domain, $x^*=1$ (Fig. S2a), and slightly decreases C_B^* at $x^*=1$, more noticeably for larger times. At $x^*=1$ C_B^* reaches the neurotoxic level at $t^*=0.5$, approximately corresponding to a time, *t*, of 7 years (Fig. S2b). The numerical solutions for C_A^* plotted in Fig. S2a closely resemble the approximate solution. In Fig. S2b, the numerical curves depicting C_B^* for larger values of D_A^* (1.12×10^7 and 1.12×10^8) coincide with the approximate solution. The unrestricted linear growth of C_B^* with time in Fig. S2b is explained by the fact that the plot does not reflect the removal of Aβ aggregates from the cytosol due to deposition into Aβ plaques. The model assumes that all aggregates are eventually integrated into the plaques.

Over extended periods, the dimensionless radius of the Aβ plaque, r_{ABP}^*, increases in proportion to the cube root of time, precisely in line with the approximate solution given by Eq. (19) (Fig. 3a). The independence of r_{ABP}^* on Aβ monomer diffusivity is explained by the model assumption of a constant rate of Aβ monomer production, with all monomers entering the CV through the left-hand side boundary, and the assumption that all Aβ aggregates produced in the CV become part of the plaques. In the initial stages of plaque growth, when t^* is in the range [0 0.01], the growth of the plaque disagrees with the cube root of time behavior. The very beginning of the plaque growth is simulated by Eq. (21), although the plaque radius later deviates from Eq. (21) and depends on t^* in a sigmoidal manner until it matches the approximate solution (Fig. 3b). The fact that Eq. (21) describes the plaque growth only at very small times is not surprising since Eq. (21) only accounts for the effect of nucleation, described by kinetic constant k_1. The sigmoidal shape of the numerically computed curve displaying $r_{ABP}^*\left(t^*\right)$ in the range of t^* between 0 and 0.01 is explained by autocatalytic growth, which takes over nucleation when enough nuclei are formed.

The independence of the plaque's radius r_{ABP}^* on D_A^* is confirmed in Fig. S3. The numerical solution coincides with the approximate solution for the scenario with $T_{1/2,A}^*\to\infty$ and $T_{1/2,B}^*\to\infty$.

3.3. Effects of varying the dimensionless rate of monomer production (the dimensionless monomer flux into the CV)

Effects of varying the dimensionless flux of Aβ monomers entering the CV through the left-hand side boundary, $q^*_{A,0}$, are investigated in Figs. 4, 5, and in Figs. S4-S6 in the Supplemental Materials.

The dimensionless concentration of Aβ monomers, C^*_A, at $x^* = 1$ and $t^*_f = 0.7$ increases with $q^*_{A,0}$ if the half-lives of Aβ monomers and aggregates are finite. If the half-lives are infinitely large, C^*_A is independent of $q^*_{A,0}$ (extra monomers are converted into aggregates) (Fig. 4a). The approximate solutions for C^*_A show little dependence on $q^*_{A,0}$. This is explained as follows. The approximate solution for C^*_A given by Eq. (S11) can be re-written as follows:

$$C^*_A = \frac{1}{\frac{1}{q^*_{A,0}} + t^*}. \tag{23}$$

As $q^*_{A,0}$ is large, the term $\frac{1}{q^*_{A,0}}$ in the denominator of Eq. (23) is negligibly small. Fig. 4 is computed for $t^* = 0.7$. Hence, Eq. (23) gives $C^*_A = 1.43$, independent of $q^*_{A,0}$ for large values of $q^*_{A,0}$. The numerical solution for C^*_A agrees with the approximate solution for the scenario with $T^*_{1/2,A} \to \infty$ and $T^*_{1/2,B} \to \infty$ (Fig. 4a).

The dimensionless concentration of Aβ aggregates, C^*_B, increases with the increase in $q^*_{A,0}$ following a power relationship (depicted as a straight line in a log-log plot). For infinite half-lives of monomers and aggregates, the neurotoxic concentration of aggregates is reached when $q^*_{A,0}$ exceeds 3×10^5, equivalent to $q_{A,0}$ of approximately 8×10^{-6} μM μm s^{-1} (Fig. 4b). The approximate solution for C^*_B is directly proportional to $q^*_{A,0}$ (refer to Eq. (S10)). The curves depicting the numerical and approximate solutions coincide for the scenario with $T^*_{1/2,A} \to \infty$ and $T^*_{1/2,B} \to \infty$.

An increase in the dimensionless flux of Aβ monomers, $q^*_{A,0}$, increases the variation in C^*_A across the CV (Fig. S4a). As discussed above, the approximate solution for C^*_A exhibits a weak dependence on $q^*_{A,0}$. The numerical solution for C^*_A agrees with the approximate solution for a small value of $q^*_{A,0}$ (4.21×10^4). However, for larger values of $q^*_{A,0}$ (4.21×10^5 and 4.21×10^6), a deviation from the lumped capacitance

conditions occurs, and C_A^* displays variations across the CV, not captured by the approximate solution. The increase in $q_{A,0}^*$ also shifts the average value of C_B^* in the CV to greater values and increases the variation in C_B^* across the CV (Fig. S4b). The numerical and approximate solutions for C_B^* coincide for smaller values of $q_{A,0}^*$ (4.21×10^4 and 4.21×10^5), while for $q_{A,0}^* = 4.21\times10^6$ the numerical solution displays a variation across the CV, deviating from the approximate solution.

The dimensionless concentration of Aβ monomers, C_A^*, at the right-hand side boundary of the domain, $x^* = 1$, exhibits an initial rapid increase followed by a gradual decrease over time (Fig. S5a). The numerical and approximate solutions in Fig. S5a nearly coincide. The dimensionless concentration of Aβ aggregates, C_B^*, at $x^* = 1$ exhibits a linear relationship with time (Fig. S5b). The neurotoxic threshold is reached faster with higher values of the monomer flux. For example, for $q_{A,0}^* = 4.21\times10^5$ the aggregate concentration C_B^* reaches the neurotoxic level at $t^* = 0.52$, which approximately corresponds to *t* of 7.5 years while for $q_{A,0}^* = 4.21\times10^6$ the aggregate concentration C_B^* reaches the neurotoxic level at $t^* = 0.06$, which approximately corresponds to *t* of 1 year (Fig. S5b). The numerical and approximate solutions agree for smaller values of $q_{A,0}^*$ (4.21×10^4 and 4.21×10^5), but some deviation is observed for $q_{A,0}^* = 4.21\times10^6$ due to the breakdown of lumped capacitance conditions.

The dimensionless radius of the Aβ plaque, r_{ABP}^*, increases proportionally to the cube root of time, in precise agreement with the approximate solution given by Eq. (19) (Fig. 5a). Note that according to Eq. (19) r_{ABP}^* is proportional to $\left(q_{A,0}^*\right)^{1/3}$. Hence, the results for different values of $q_{A,0}^*$ in Fig. 5a are different. However, for each value of $q_{A,0}^*$ the numerical and analytical solutions coincide at large times. In contrast, for small times (when t^* falls within the range [0 0.02] for $q_{A,0}^* = 4.21\times10^4$, [0 0.01] for $q_{A,0}^* = 4.21\times10^5$, and [0 0.005] for $q_{A,0}^* = 4.21\times10^6$), the numerical solution deviates from the analytical one. In these small time ranges the numerical solution displays a sigmoidal increase in the plaque's radius, consistent with observations in [33].

Confirmation of the power relationship between r_{ABP}^* and $q_{A,0}^*$ is presented in Fig. S6 (with the power on $q_{A,0}^*$ being 1/3). The numerical and approximate solutions in Fig. S6 coincide for the scenario with $T_{1/2,A}^* \to \infty$ and $T_{1/2,B}^* \to \infty$.

3.4. Effects of varying the dimensionless half-life of Aβ monomers

Effects of varying the dimensionless half-life of Aβ monomers, $T^*_{1/2,A}$, are investigated in Figs. 6, 7, and in Figs. S7-S9 in the Supplemental Materials.

The dimensionless concentration of Aβ monomers, C^*_A, at $x^* = 1$ and $t^*_f = 0.7$ increases with the increase in $T^*_{1/2,A}$ until C^*_A reaches a constant value, for the case with a finite half-life of Aβ aggregates, $T^*_{1/2,B}$. In contrast, for the case with the infinite half-life of Aβ aggregates, $T^*_{1/2,B}$, C^*_A initially increases with the increase in $T^*_{1/2,A}$ and then decreases to a constant value (Fig. 6a). The dimensionless concentration of Aβ aggregates, C^*_B, increases with the increase in $T^*_{1/2,A}$ until reaching a constant value. In the infinite half-life of Aβ aggregates scenario, the neurotoxic concentration of aggregates is reached when $T^*_{1/2,A}$ exceeds 10^{-4}, equivalent to $T_{1/2,A}$ of around 5×10^4 s (Fig. 6b). The approximate solution is independent of the values of $T^*_{1/2,A}$ and $T^*_{1/2,B}$ (because it is obtained under the assumption that $T^*_{1/2,A} \to \infty$ and $T^*_{1/2,B} \to \infty$). Numerical solutions for C^*_A and C^*_B obtained for $T^*_{1/2,B} \to \infty$ approach the respective approximate solutions when $T^*_{1/2,A} > 10^{-3}$ in Fig. 6a and 6b.

$T^*_{1/2,A}$ has no effect on variations of C^*_A and C^*_B across the CV (Fig. S7). Since the approximate solution is derived for $T^*_{1/2,A} \to \infty$ and $T^*_{1/2,B} \to \infty$, there is a slight discrepancy between the numerical and approximate solutions for C^*_A and C^*_B even for the largest value of $T^*_{1/2,A}$ (1.02×10^{-4}) (Fig. S7).

The effect of $T^*_{1/2,A}$ on the dimensionless concentration of Aβ monomers, C^*_A, at the right-hand side boundary of the domain, $x^* = 1$, depends on the value of $T^*_{1/2,A}$. For large $T^*_{1/2,A}$ (1.02×10^{-4}), C^*_A exhibits a rapid increase from zero (a value that is dictated by the initial condition in Eq. (10a)) followed by a gradual decrease over time. Conversely, for smaller $T^*_{1/2,A}$ (1.02×10^{-5} and 1.02×10^{-6}), C^*_A quickly increases from zero to a constant value, with the constant value being smaller for smaller $T^*_{1/2,A}$ (Fig. S8a). The effect of $T^*_{1/2,A}$ on the dimensionless concentration of Aβ aggregates, C^*_B, at the right-hand side boundary of the domain, $x^* = 1$, also depends on the value of $T^*_{1/2,A}$. A large value of $T^*_{1/2,A}$ (1.02×10^{-4}) results in an increase in C^*_B until C^*_B reaches a neurotoxic concentration at $t^* = 0.7$, corresponding to 10

years. However, for smaller values of $T^*_{1/2,A}$ (1.02×10^{-5} and 1.02×10^{-6}), C^*_B remains close to zero (Fig. S8b). Some discrepancy between the numerical and approximate solutions in Fig. S8, even for the largest value of $T^*_{1/2,A}$ (1.02×10^{-4}), is attributed to the fact that this value of $T^*_{1/2,A}$ is still insufficiently close to infinity.

The dimensionless radius of the Aβ plaque, r^*_{ABP}, increases with the increase of dimensionless time, t^*, yet even for the largest value of $T^*_{1/2,A}$ (1.02×10^{-4}) it remains below the curve depicting the approximate solution (19) (Fig. 7a). The validity of the approximate solution is limited to infinitely long half-lives of Aβ monomers and aggregates. As the decay of monomers results in less conversion of monomers into aggregates, it leads to fewer aggregates being incorporated into the plaques. At the rates of Aβ monomer degradation used to compute Fig. 7, the plaque grows slowly at small t^*, slower for smaller values of $T^*_{1/2,A}$ (Fig. 7b).

Fig. S9 demonstrates that for the case of an infinite half-life of Aβ aggregates, the dimensionless plaque radius reaches that predicted by the approximate solution when $T^*_{1/2,A}$ exceeds 10^{-3}, which approximately corresponds to $T_{1/2,A}$ of 4.5×10^5 s.

3.5. Effects of varying the dimensionless half-life of Aβ aggregates

Effects of varying the dimensionless half-life of Aβ aggregates, $T^*_{1/2,B}$, are investigated in Figs. 8, 9, and in Figs. S10-S13 in the Supplemental Materials.

The dimensionless concentration of Aβ monomers, C^*_A, at $x^*=1$ and $t^*_f=0.7$ decreases with the increase in $T^*_{1/2,B}$, for the case with the infinite half-life of Aβ monomers, $T^*_{1/2,A}$. However, for the scenario with a finite half-life of Aβ monomers, $T^*_{1/2,A}$, C^*_A remains constant (Fig. 8a). The dimensionless concentration of Aβ aggregates, C^*_B, increases with the increase in $T^*_{1/2,A}$. In the case of an infinite half-life of Aβ monomers, the neurotoxic concentration of aggregates is reached when $T^*_{1/2,B}$ exceeds 1, approximately corresponding to $T_{1/2,B}$ of around 4.5×10^8 s (Fig. 8b). In Fig. 8, both C^*_A and C^*_B approach the approximate solution for the scenario with $T^*_{1/2,A}\to\infty$ when $T^*_{1/2,B}>1$.

The parameter $T^*_{1/2,B}$ has no effect on variations in C^*_A and C^*_B across the CV (Fig. S10). The dimensionless concentration of Aβ monomers, C^*_A, at the right-hand side boundary of the domain, $x^* = 1$, gradually increases with time until it reaches a constant value, which is larger for a smaller half-life of Aβ aggregates, $T^*_{1/2,B}$ (Fig. S11a). The dimensionless concentration of Aβ aggregates, C^*_B, at the right-hand side boundary of the domain, $x^* = 1$, remains much smaller than the neurotoxic concentration. It also stays significantly below the curve representing the approximate solution for C^*_B, even for the largest value of $T^*_{1/2,B}$ (5.12×10^{-4}) (Fig. S11b).

The dimensionless radius of the Aβ plaque, r^*_{ABP}, increases with an increase in the dimensionless time, t^*. However, even for the largest value of $T^*_{1/2,B}$ (5.12×10^{-4}), it remains much below the curve predicted by the approximate solution (Eq. 19) (Fig. 9a). Interestingly, for small times, the curve depicting the case with $T^*_{1/2,B} = 5.12\times10^{-4}$ oscillates in the range of t^* between 0 and 0.03 (Fig. 9b). To verify that this is not a numerical artifact, computations were repeated on a mesh ten times finer with respect to t^* and x^*. The result displayed in Fig. S12 shows an oscillatory behavior identical to that displayed in Fig. 9b. Additionally, Fig. S13 shows that for the case of an infinite half-life of Aβ monomers, the dimensionless plaque radius reaches the value predicted by the approximate solution when $T^*_{1/2,B}$ exceeds 2.2, corresponding to $T_{1/2,B}$ of 10^9 s.

4. Discussion, model limitations, and future directions

This study introduces a model that simulates the diffusion of Aβ monomers, the conversion of monomers into aggregates, and the formation of senile plaques. The density of Aβ plaque is assumed to be 1.35 g/cm³, and the growth time of an Aβ plaque is set at 10 years. Under these conditions the model involves four dimensionless parameters: (1) the dimensionless diffusivity of Aβ monomers, (2) the dimensionless flux of Aβ monomers into the CV due to monomer production on lipid membranes, (3) the dimensionless half-life of Aβ monomers, and (4) the dimensionless half-life of Aβ aggregates.

Given the nonlinear nature of the governing equations, the relationships between the solutions and the parameters are complex, as anticipated for nonlinear problems. Key observations and insights are summarized below.

The guidance on how the solution depends on the dimensionless parameters is provided by the approximate solution. The approximate solution is given by Eq. (S10), providing the concentration of aggregates, C_B^*; Eq. (S11), providing the concentration of monomers, C_A^*; and Eq. (19), specifying the plaque radius, r_{ABP}^*. The approximate solution indicates that, over extended periods, aggregate concentration linearly increases with t^* while monomer concentration decreases proportionally to $1/t^*$. C_B^* is directly proportional to the monomer flux, $q_{A,0}^*$, while C_A^* is independent of $q_{A,0}^*$ for large t^*. These trends are observed in Figs. 4 and S5. The plaque radius is proportional to the cube root of time. For a fixed density ρ^*, r_{ABP}^* only depends on the flux of monomers into the CV, $q_{A,0}^*$; it is proportional to $\left(q_{A,0}^*\right)^{1/3}$. These trends are observed in Figs. 5 and S6.

However, the approximate solution has limitations stemming from two assumptions used to obtain it: (i) the lumped capacitance approximation, where variations in concentrations of Aβ monomers and aggregates across the CV are considered negligible, and concentrations depend solely on time, and (ii) the assumption of dysfunctional protein degradation machinery, implying infinitely large half-lives for Aβ monomers and aggregates.

The lumped capacitance model might fail when the diffusivity of Aβ monomers is small (Figs. 2 and S1). Notably, for the lumped capacitance model to break down due to small diffusivity of Aβ monomers, it must be an order of magnitude less than its physiological value. In essence, with the physiological value of the monomer diffusivity, Aβ plaque formation is not diffusion-controlled. The lumped capacitance model may also fail for very large fluxes of Aβ monomers into the CV (Fig. S4).

The assumption of infinite half-lives for Aβ monomers and aggregates is more restrictive. Reducing $T_{1/2,A}^*$ and $T_{1/2,B}^*$ from infinite to physiological values results in significant deviations from the approximate solution (Figs. 6-9). For finite half-lives of Aβ monomers and/or aggregates the Aβ plaque radius does not grow indefinitely with time, which agrees with the existence of the saturation state reported in [34]. The plaque radius stabilizes once it reaches a certain value dependent on the half-life of monomers/aggregates (Fig. 9). For finite half-lives of monomers and aggregates, the solution's dependence on parameters becomes more complex, involving all four parameters: $q_{A,0}^*$, D_A^*, $T_{1/2,A}^*$, and $T_{1/2,B}^*$ (while the approximate solution depends only on $q_{A,0}^*$, see Eqs. (S10), (S11), and (19)).

The model developed in this study has limitations as it does not simulate the process of Aβ aggregate assembly into plaques. Instead, the model assumes that all aggregates produced in the CV are absorbed by

the plaque. Thus, calculating the rate of production of aggregates makes it possible to simulate the growth of the plaque. Future research should focus on simulating the assembly of aggregates into plaques. Investigating scenarios where new plaques deposit close to existing ones, forming plaque clusters as suggested by [35], is important. Additionally, simulating the age-related increase in the number of plaques [35] is a crucial avenue for future exploration.

Data accessibility. This article has no additional data.

Authors' contributions. AVK is the sole author of this paper.

Competing interests. The author declares no competing interests.

Funding statement. AVK acknowledges the support provided by the National Science Foundation (grant CBET-2042834) and the Alexander von Humboldt Foundation through the Humboldt Research Award.

References

1. Hardy J. 2006 A hundred years of Alzheimer's disease research. *Neuron* **52,** 3-13. (doi:10.1016/j.neuron.2006.09.016)

2. Maqbool M, Mobashir M, Hoda N. 2016 Pivotal role of glycogen synthase kinase-3: A therapeutic target for Alzheimer's disease. *Eur. J. Med. Chem.* **107,** 63-81. (doi:10.1016/j.ejmech.2015.10.018)

3. Hung S, Fu W. 2017 Drug candidates in clinical trials for Alzheimer's disease. *J. Biomed. Sci.* **24,** 47. (doi:10.1186/s12929-017-0355-7)

4. Nalivaeva NN, Turner AJ. 2013 The amyloid precursor protein: A biochemical enigma in brain development, function and disease. *FEBS Lett.* **587,** 2046-2054. (doi:10.1016/j.febslet.2013.05.010)

5. Murphy MP, LeVine H3. 2010 Alzheimer's disease and the amyloid-beta peptide. *J. Alzheimers Dis.* **19,** 311-323. (doi:10.3233/JAD-2010-1221)

6. Knopman DS, Amieva H, Petersen RC, Chételat G, Holtzman DM, Hyman BT, Nixon RA, Jones DT. 2021 Alzheimer disease. *Nature Reviews Disease Primers* **7,** 33. (doi:10.1038/s41572-021-00269-y)

7. Hardy J, Selkoe DJ. 2002 The amyloid hypothesis of Alzheimer's disease: Progress and problems on the road to therapeutics. *Science* **297,** 353-356. (doi:10.1126/science.1072994)

8. O'Brien RJ, Wong PC. 2011 Amyloid precursor protein processing and Alzheimer's disease. *Annual Review of Neuroscience, Vol 34* **34,** 185-204. (doi:10.1146/annurev-neuro-061010-113613)

9. Selkoe DJ, Hardy J. 2016 The amyloid hypothesis of Alzheimer's disease at 25years. *EMBO Molecular Medicine* **8,** 595-608. (doi:10.15252/emmm.201606210)

10. Huang Y, Happonen KE, Burrola PG, O'Connor C, Hah N, Huang L, Nimmerjahn A, Lemke G. 2021 Microglia use TAM receptors to detect and engulf amyloid β plaques. *Nat. Immunol.* **22,** 586-594. (doi:10.1038/s41590-021-00913-5)

11. Yada Y, Naoki H. 2023 Few-shot prediction of amyloid β accumulation from mainly unpaired data on biomarker candidates. *NPJ Systems Biology and Applications* **9,** 59. (doi:10.1038/s41540-023-00321-5)

12. Jagust WJ, Landau SM, Alzheimer's Disease Neuroimaging Initiative. 2021 Temporal dynamics of β-amyloid accumulation in aging and Alzheimer disease. *Neurology* **96,** e1347-e1357. (doi:10.1212/WNL.0000000000011524)

13. Chen G, Xu T, Yan Y, Zhou Y, Jiang Y, Melcher K, Xu HE. 2017 Amyloid beta: Structure, biology and structure-based therapeutic development. *Acta Pharmacol. Sin.* **38,** 1205-1235. (doi:10.1038/aps.2017.28)

14. Hampel H, Hardy J, Blennow K, Chen C, Perry G, Kim SH, Villemagne VL, Aisen P, Vendruscolo M, Iwatsubo T, Masters CL, Cho M, Lannfelt L, Cummings JL, Vergallo A. 2021 The amyloid-β pathway in Alzheimer's disease. *Mol. Psychiatry* **26,** 5481-5503. (doi:10.1038/s41380-021-01249-0)

15. Waters J. 2010 The concentration of soluble extracellular amyloid-beta protein in acute brain slices from CRND8 mice. *PLOS One* **5,** e15709. (doi:10.1371/journal.pone.0015709)

16. Bora RP, Prabhakara R. 2009 Translational, rotational and internal dynamics of amyloid beta-peptides (A beta 40 and A beta 42) from molecular dynamics simulations. *J. Chem. Phys.* **131,** 155103. (doi:10.1063/1.3249609)

17. Rahman MM, Lendel C. 2021 Extracellular protein components of amyloid plaques and their roles in Alzheimer's disease pathology. *Molecular Neurodegeneration* **16,** 59. (doi:10.1186/s13024-021-00465-0)

18. Morris AM, Watzky MA, Agar JN, Finke RG. 2008 Fitting neurological protein aggregation kinetic data via a 2-step, minimal/"ockham's razor" model: The Finke-Watzky mechanism of nucleation followed by autocatalytic surface growth. *Biochemistry* **47,** 2413-2427. (doi:10.1021/bi701899y)

19. Iashchishyn IA, Sulskis D, Nguyen Ngoc M, Smirnovas V, Morozova-Roche LA. 2017 Finke-Watzky two-step nucleation-autocatalysis model of S100A9 amyloid formation: Protein misfolding as "nucleation" event. *ACS Chem. Neurosci.* **8,** 2152-2158. (doi:10.1021/acschemneuro.7b00251)

20. Kuznetsov AV. 2023 Effect of diffusivity of amyloid beta monomers on the formation of senile plaques. *bioRxiv* 2023.07.31.551367. (doi:10.1101/2023.07.31.551367)

21. Kuznetsov AV. 2023 Numerical and analytical simulation of the growth of amyloid-β plaques. *bioRxiv* 2023.09.11.557187. (doi:10.1101/2023.09.11.557187)

22. Haass C, Kaether C, Thinakaran G, Sisodia S. 2012 Trafficking and proteolytic processing of APP. *Cold Spring Harb Perspect. Med.* **2,** a006270. (doi:10.1101/cshperspect.a006270)

23. Masters CL, Selkoe DJ. 2012 Biochemistry of amyloid β-protein and amyloid deposits in Alzheimer disease. *Cold Spring Harb Perspect. Med.* **2,** a006262. (doi:10.1101/cshperspect.a006262)

24. Raskatov JA. 2019 What is the "Relevant" amyloid β42 concentration? *ChemBioChem* **20,** 1725-1726. (doi:10.1002/cbic.201900097)

25. Bieschke J, Zhang Q, Powers ET, Lerner RA, Kelly JW. 2005 Oxidative metabolites accelerate Alzheimer's amyloidogenesis by a two-step mechanism, eliminating the requirement for nucleation. *Biochemistry* **44,** 4977-4983. (doi:10.1021/bi0501030)

26. Querol-Vilaseca M, Colom-Cadena M, Pegueroles J, Nuñez-Llaves R, Luque-Cabecerans J, Muñoz-Llahuna L, Andilla J, Belbin O, Spires-Jones T, Gelpi E, Clarimon J, Loza-Alvarez P, Fortea J, Lleó A. 2019 Nanoscale structure of amyloid-β plaques in Alzheimer's disease. *Scientific Reports* **9,** 5181. (doi:10.1038/s41598-019-41443-3)

27. Holtzman DM, Morris JC, Goate AM. 2011 Alzheimer's disease: The challenge of the second century. *Science Translational Medicine* **3,** 77sr1. (doi:10.1126/scitranslmed.3002369)

28. Cavicchi RE, King J, Ripple DC. 2018 Measurement of average aggregate density by sedimentation and brownian motion analysis. *J. Pharm. Sci.* **107,** 1304-1312. (doi:10.1016/j.xphs.2018.01.013)

29. Dawkins E, Derks RJE, Schifferer M, Trambauer J, Winkler E, Simons M, Paquet D, Giera M, Kamp F, Steiner H. 2023 Membrane lipid remodeling modulates γ-secretase processivity. *J. Biol. Chem.* **299,** (doi:10.1016/j.jbc.2023.103027)

30. Hori Y, Takeda S, Cho H, Wegmann S, Shoup TM, Takahashi K, Irimia D, Elmaleh DR, Hyman BT, Hudry E. 2015 A food and drug administration-approved asthma therapeutic agent impacts amyloid β in the brain in a transgenic model of Alzheimer disease. *J. Biol. Chem.* **290,** 1966-1978. (doi:10.1074/jbc.M114.586602)

31. Kostylev MA, Kaufman AC, Nygaard HB, Patel P, Haas LT, Gunther EC, Vortmeyer A, Strittmatter SM. 2015 Prion-protein-interacting amyloid-β oligomers of high molecular weight are tightly correlated with memory impairment in multiple Alzheimer mouse models. *J. Biol. Chem.* **290,** 17415-17438. (doi:10.1074/jbc.M115.643577)

32. Watzky MA, Finney EE, Finke RG. 2008 Transition-metal nanocluster size vs formation time and the catalytically effective nucleus number: A mechanism-based treatment. *J. Am. Chem. Soc.* **130,** 11959-11969. (doi:10.1021/ja8017412)

33. Burgold S, Filser S, Dorostkar MM, Schmidt B, Herms J. 2014 In vivo imaging reveals sigmoidal growth kinetic of β-amyloid plaques. *Acta Neuropathologica Communications* **2,** 30. (doi:10.1186/2051-5960-2-30)

34. Serrano-Pozo A, Mielke ML, Muzitansky A, Gómez-Isla T, Growdon JH, Bacskai BJ, Betensky RA, Frosch MP, Hyman BT. 2012 Stable size distribution of amyloid plaques over the course of Alzheimer disease. *J. Neuropathol. Exp. Neurol.* **71,** 694-701. (doi:10.1097/NEN.0b013e31825e77de)

35. McCarter JF, Liebscher S, Bachhuber T, Abou-Ajram C, Hübener M, Hyman BT, Haass C, Meyer-Luehmann M. 2013 Clustering of plaques contributes to plaque growth in a mouse model of Alzheimer's disease. *Acta Neuropathol.* **126,** 179-188. (doi:10.1007/s00401-013-1137-2)

36. Cruz L, Urbanc B, Buldyrev SV, Christie R, Gómez-Isla T, Havlin S, McNamara M, Stanley HE, Hyman BT. 1997 Aggregation and disaggregation of senile plaques in Alzheimer disease. *Proc. Natl. Acad. Sci. U. S. A.* **94,** 7612-7616. (doi:10.1073/pnas.94.14.7612)

37. Kuznetsov IA, Kuznetsov AV. 2022 An analytical solution simulating growth of Lewy bodies. *Math. Med. Biol.* **39,** 299-312. (doi:10.1093/imammb/dqac006)

Figure captions

Fig. 1. A schematic diagram illustrating two CVs. An Aβ plaque forms at the interface between the CVs. Aβ monomers enter the CV from one of its faces, and Aβ aggregates are produced through a combined process of nucleation and autocatalytic growth. Aβ monomers are generated at a lipid membrane (assumed at the x=0 boundary). The x=L boundary is modeled as symmetric, resulting in no monomer flux through it.

Fig. 2. Dimensionless molar concentration of Aβ monomers, C_A^* (a), and Aβ aggregates, C_B^* (b), plotted against the dimensionless diffusivity of Aβ monomers, D_A^*. Approximate solutions for C_A^* and C_B^* are computed using Eqs. (S11) and (S10), respectively. The computational results are presented at the right-hand side boundary of the CV, $x^* = 1$, at $t_f^* = 0.7$ (10 years).

Fig. 3. (a) Dimensionless radius of a growing Aβ plaque, r_{ABP}^*, as a function of dimensionless time, t^*. (b) Similar to Fig. 3a, but focusing on the time range [0 0.07] on the x-axis. The approximate solution for r_{ABP}^* is plotted using Eq. (19); r_{ABP}^* is directly proportional to $\left(t^*\right)^{1/3}$. These computational results are presented at the right-hand side boundary of the CV, $x^* = 1$, and correspond to the scenario with an infinite half-life of Aβ monomers and aggregates, $T_{1/2,A}^* \to \infty$ and $T_{1/2,B}^* \to \infty$, respectively. Results are shown for three values of the dimensionless diffusivity of Aβ monomers, D_A^*.

Fig. 4. Dimensionless molar concentrations of Aβ monomers, C_A^* (a), and Aβ aggregates, C_B^* (b), plotted against the dimensionless flux of Aβ monomers from the left-hand side boundary of the CV, $q_{A,0}^*$. Approximate solutions for C_A^* and C_B^* are computed using Eqs. (S11) and (S10), respectively. The approximate solution for C_B^* is directly proportional to $\left(q_{A,0}^*\right)^{1/3}$. The computational results are presented at the right-hand side boundary of the CV, $x^* = 1$, at $t_f^* = 0.7$ (10 years).

Fig. 5. (a) Dimensionless radius of a growing Aβ plaque, r_{ABP}^*, as a function of dimensionless time, t^*. (b) Similar to Fig. 5a, but focusing on the time range [0 0.07] on the x-axis. The approximate solution for r_{ABP}^* is plotted using Eq. (19); r_{ABP}^* is directly proportional to $\left(t^*\right)^{1/3}$. These computational results are presented at the right-hand side boundary of the CV, $x^* = 1$, and correspond to the scenario with an infinite half-life of Aβ monomers and aggregates, $T_{1/2,A}^* \to \infty$ and $T_{1/2,B}^* \to \infty$, respectively. Results are

shown for three values of the dimensionless flux of Aβ monomers from the left-hand side boundary of the CV, $q^*_{A,0}$.

Fig. 6. Dimensionless molar concentration of Aβ monomers, C^*_A (a), and Aβ aggregates, C^*_B (b), plotted against the dimensionless half-life of Aβ monomers, $T^*_{1/2,A}$. Approximate solutions for C^*_A and C^*_B are computed using Eqs. (S11) and (S10), respectively. The computational results are presented at the right-hand side boundary of the CV, $x^* = 1$, at $t^*_f = 0.7$ (10 years).

Fig. 7. (a) Dimensionless radius of a growing Aβ plaque, r^*_{ABP}, as a function of dimensionless time, t^*. (b) Similar to Fig. 7a, focusing on the time range [0 0.07] on the *x*-axis. The approximate solution for r^*_{ABP} is plotted using Eq. (19); r^*_{ABP} is directly proportional to $\left(t^*\right)^{1/3}$. These computational results are presented at the right-hand side boundary of the CV, $x^* = 1$, and correspond to the scenario with an infinite half-life of Aβ aggregates, $T^*_{1/2,B} \to \infty$. Results are shown for three values of the dimensionless half-life of Aβ monomers, $T^*_{1/2,A}$.

Fig. 8. Dimensionless molar concentration of Aβ monomers, C^*_A (a), and Aβ aggregates, C^*_B (b), plotted against the dimensionless half-life of Aβ aggregates, $T^*_{1/2,B}$. Approximate solutions for C^*_A and C^*_B are computed using Eqs. (S11) and (S10), respectively. The computational results are presented at the right-hand side boundary of the CV, $x^* = 1$, at $t^*_f = 0.7$ (10 years).

Fig. 9. (a) Dimensionless radius of a growing Aβ plaque, r^*_{ABP}, as a function of dimensionless time, t^*. (b) Similar to Fig. 9a, but focusing on the time range [0 0.07] on the *x*-axis. The approximate solution for r^*_{ABP} is plotted using Eq. (19); r^*_{ABP} is directly proportional to $\left(t^*\right)^{1/3}$. These computational results are presented at the right-hand side boundary of the CV, $x^* = 1$, and correspond to the scenario with an infinite half-life of Aβ monomers, $T^*_{1/2,A} \to \infty$. Results are shown for three values of the dimensionless half-life of Aβ aggregates, $T^*_{1/2,B}$.

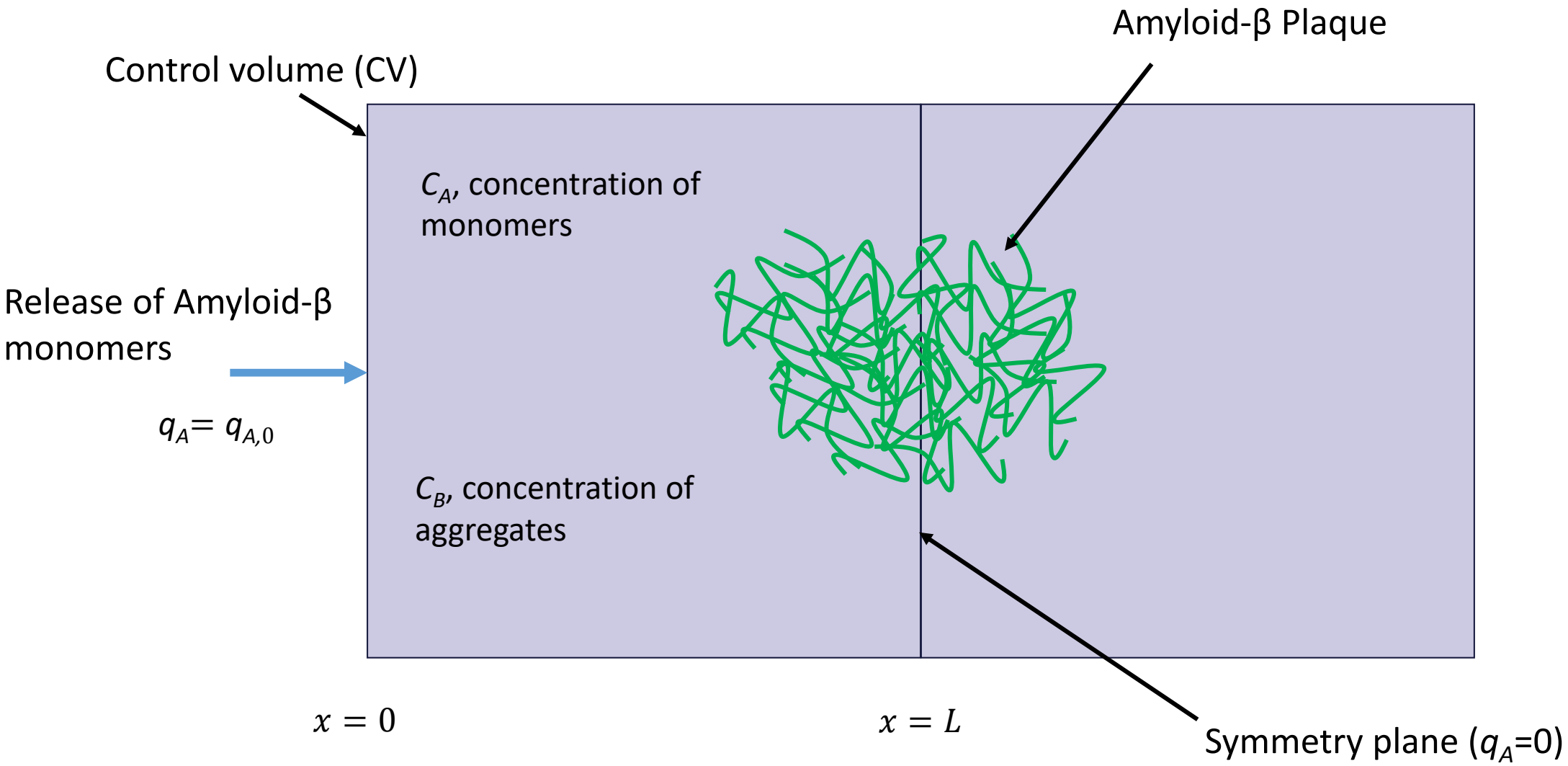
Amyloid-β Plaque
Control volume (CV)
C_A, concentration of monomers
Release of Amyloid-β monomers
$q_A = q_{A,0}$
C_B, concentration of aggregates
$x = 0$
$x = L$
Symmetry plane (q_A=0)

Figure 1

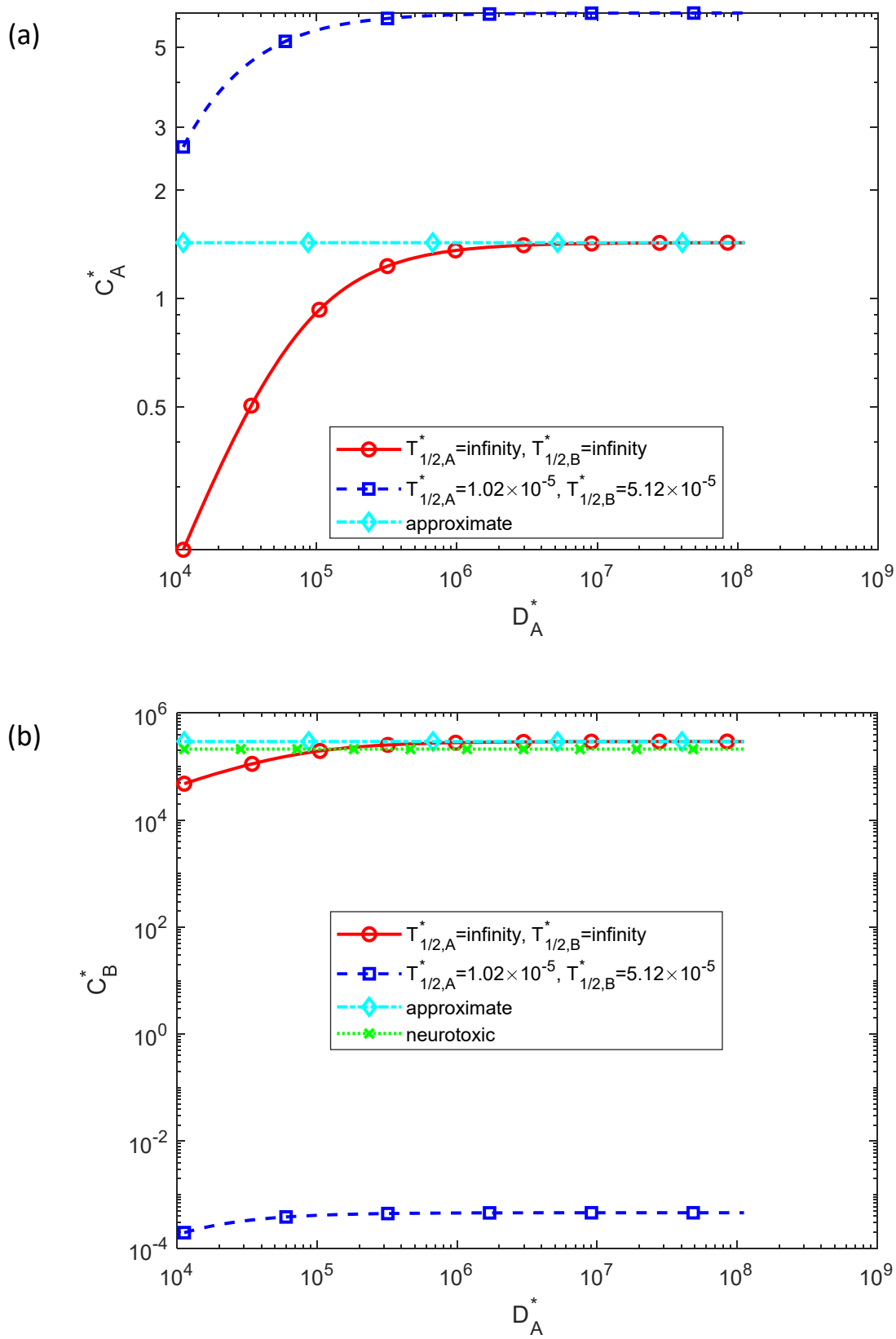
(a)
5
3
2
1
0.5
C^*_A
$T^*_{1/2,A}$=infinity, $T^*_{1/2,B}$=infinity
$T^*_{1/2,A}=1.02\times10^{-5}$, $T^*_{1/2,B}=5.12\times10^{-5}$
approximate
10^4
10^5
10^6
10^7
10^8
10^9
D^*_A
(b)
10^6
10^4
10^2
10^0
10^{-2}
10^{-4}
C^*_B
$T^*_{1/2,A}$=infinity, $T^*_{1/2,B}$=infinity
$T^*_{1/2,A}=1.02\times10^{-5}$, $T^*_{1/2,B}=5.12\times10^{-5}$
approximate
neurotoxic
10^4
10^5
10^6
10^7
10^8
10^9
D^*_A

Figure 2

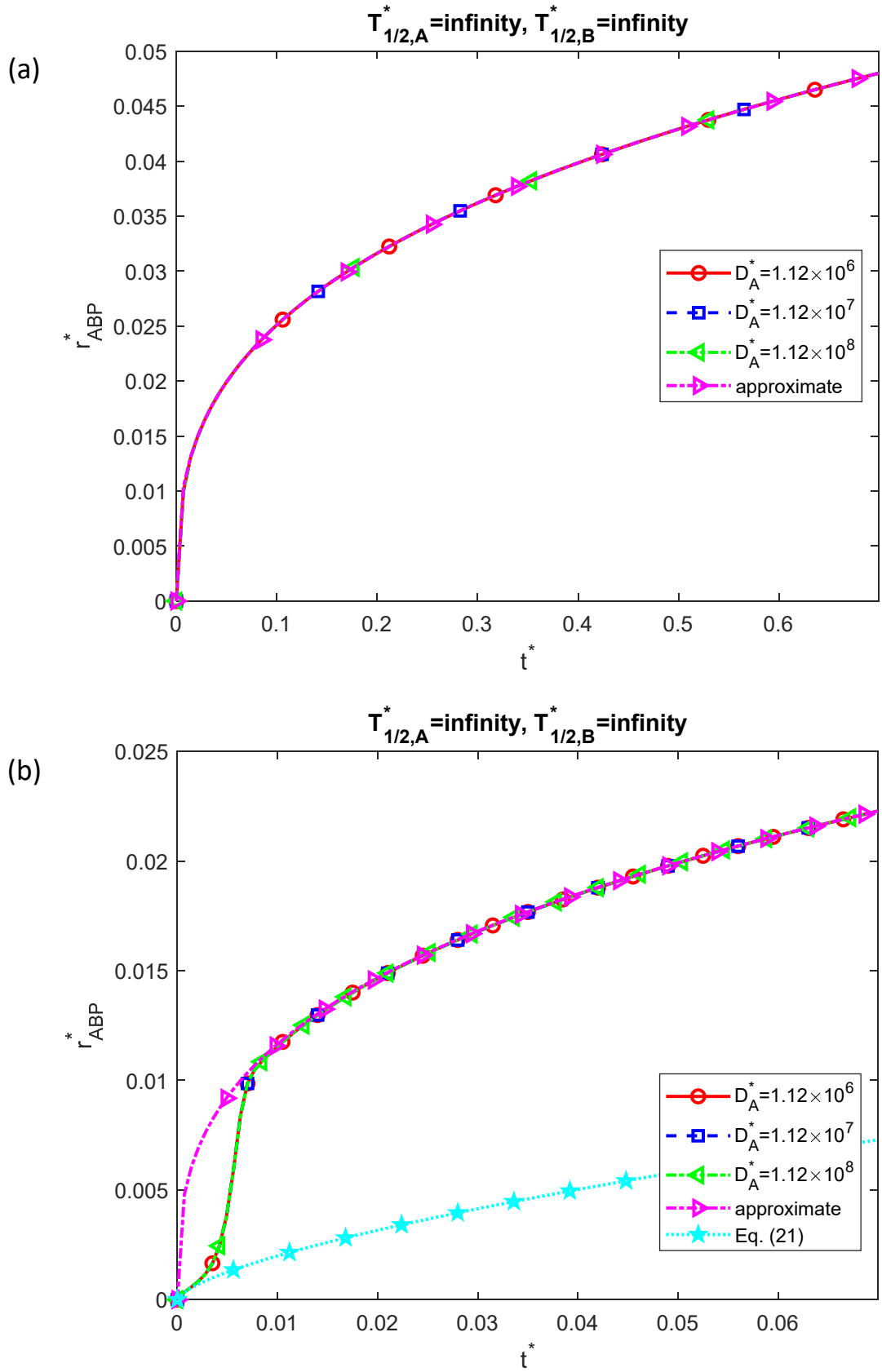
(a)
T*1/2,A=infinity, T*1/2,B=infinity
r*ABP
t*
D*A=1.12×10^6
D*A=1.12×10^7
D*A=1.12×10^8
approximate
(b)
T*1/2,A=infinity, T*1/2,B=infinity
r*ABP
t*
D*A=1.12×10^6
D*A=1.12×10^7
D*A=1.12×10^8
approximate
Eq. (21)

Figure 3

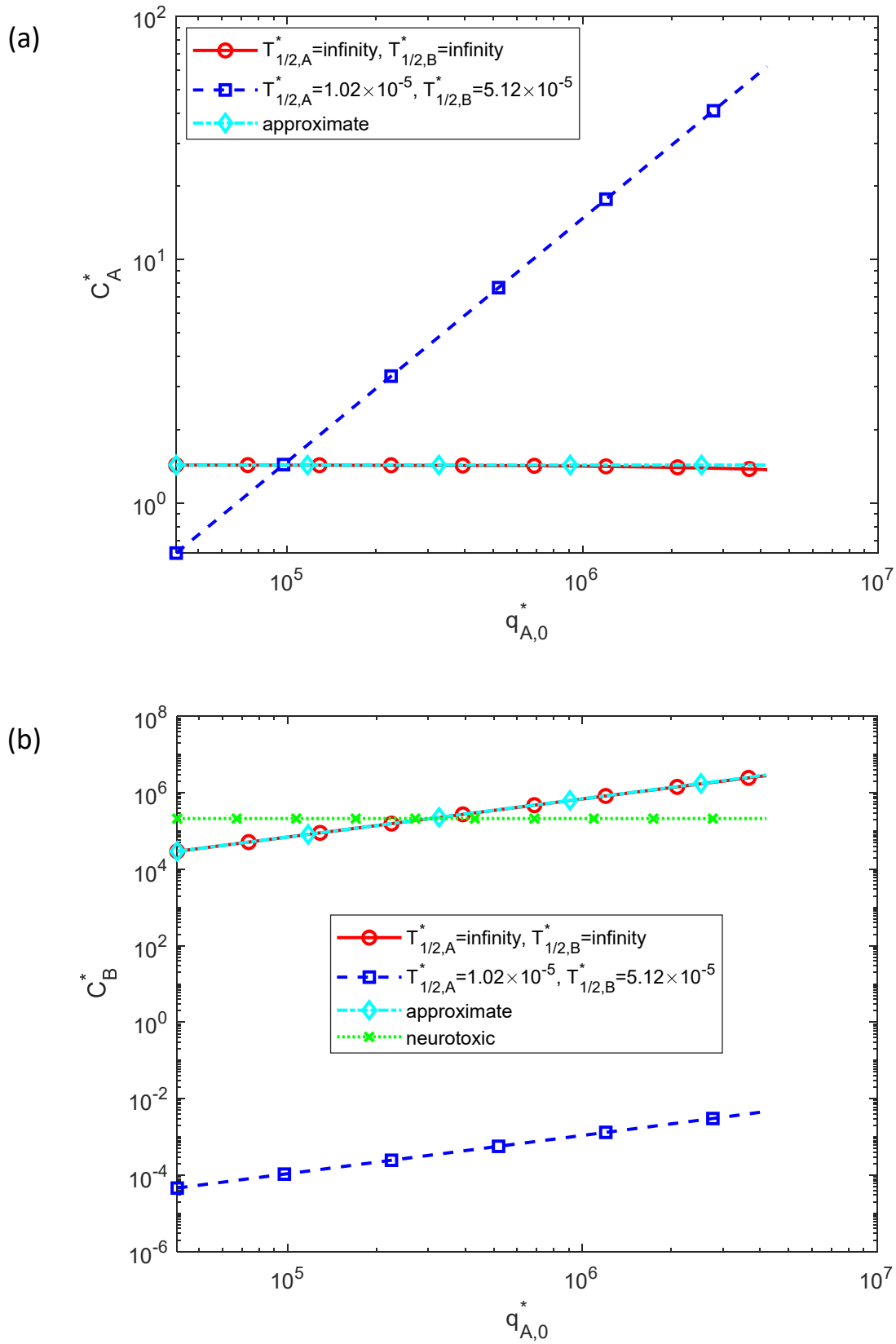
(a)
$T^*_{1/2,A}$=infinity, $T^*_{1/2,B}$=infinity
$T^*_{1/2,A}=1.02\times10^{-5}$, $T^*_{1/2,B}=5.12\times10^{-5}$
approximate
C^*_A
$q^*_{A,0}$
(b)
$T^*_{1/2,A}$=infinity, $T^*_{1/2,B}$=infinity
$T^*_{1/2,A}=1.02\times10^{-5}$, $T^*_{1/2,B}=5.12\times10^{-5}$
approximate
neurotoxic
C^*_B
$q^*_{A,0}$

Figure 4

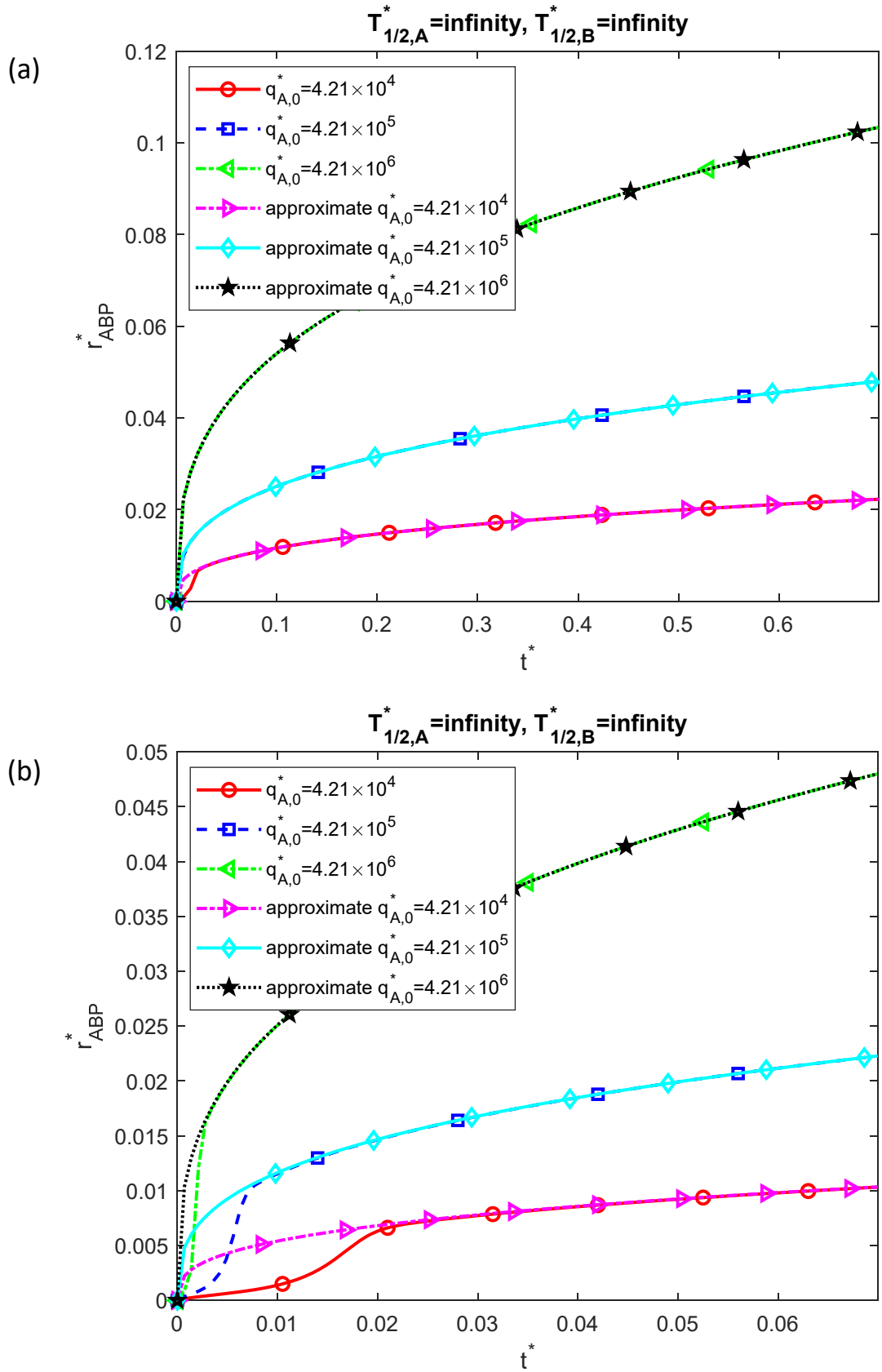
(a)
T*1/2,A=infinity, T*1/2,B=infinity
q*A,0=4.21×10^4
q*A,0=4.21×10^5
q*A,0=4.21×10^6
approximate q*A,0=4.21×10^4
approximate q*A,0=4.21×10^5
approximate q*A,0=4.21×10^6
r*ABP
t*
0
0.02
0.04
0.06
0.08
0.1
0.12
0.1
0.2
0.3
0.4
0.5
0.6
(b)
T*1/2,A=infinity, T*1/2,B=infinity
q*A,0=4.21×10^4
q*A,0=4.21×10^5
q*A,0=4.21×10^6
approximate q*A,0=4.21×10^4
approximate q*A,0=4.21×10^5
approximate q*A,0=4.21×10^6
r*ABP
t*
0
0.005
0.01
0.015
0.02
0.025
0.03
0.035
0.04
0.045
0.05
0.01
0.02
0.03
0.04
0.05
0.06

Figure 5

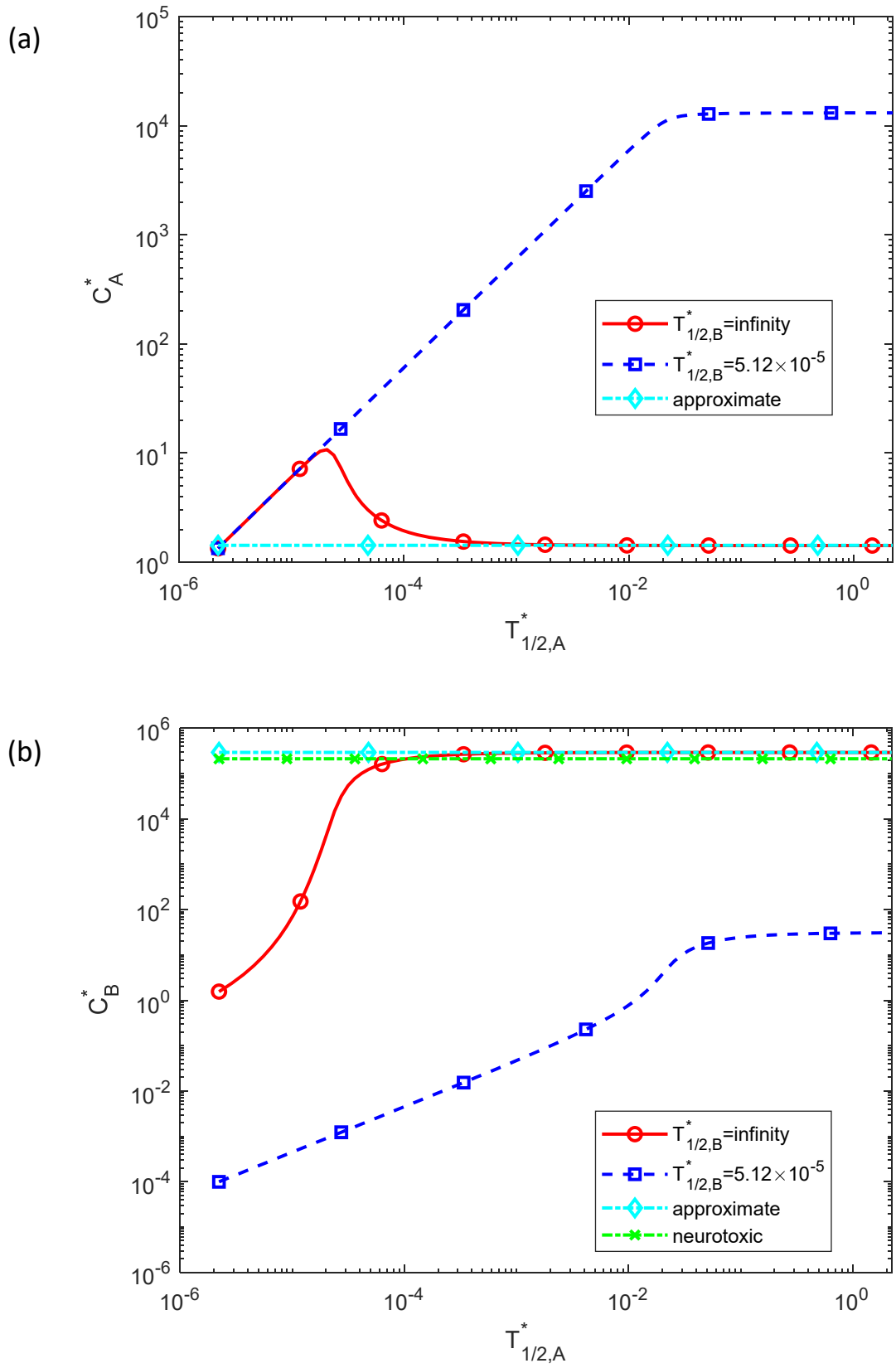
(a)
10^5
10^4
10^3
10^2
10^1
10^0
C^*_A
10^{-6}
10^{-4}
10^{-2}
10^0
$T^*_{1/2,A}$
$T^*_{1/2,B}$=infinity
$T^*_{1/2,B}$=5.12×10^{-5}
approximate
(b)
10^6
10^4
10^2
10^0
10^{-2}
10^{-4}
10^{-6}
C^*_B
10^{-6}
10^{-4}
10^{-2}
10^0
$T^*_{1/2,A}$
$T^*_{1/2,B}$=infinity
$T^*_{1/2,B}$=5.12×10^{-5}
approximate
neurotoxic

Figure 6

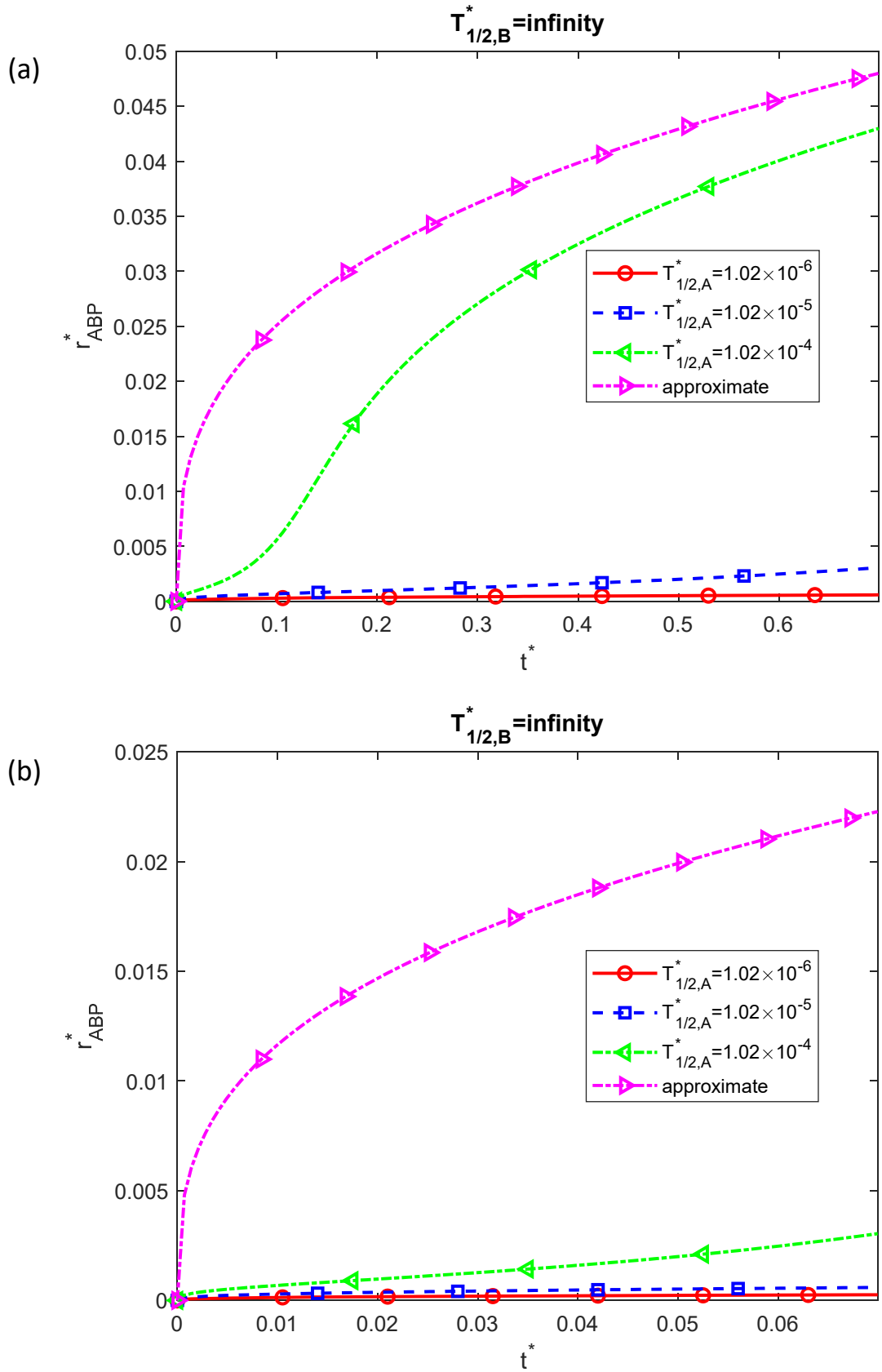
(a)
T*1/2,B=infinity
0.05
0.045
0.04
0.035
0.03
0.025
0.02
0.015
0.01
0.005
0
r*ABP
0
0.1
0.2
0.3
0.4
0.5
0.6
t*
T*1/2,A=1.02×10-6
T*1/2,A=1.02×10-5
T*1/2,A=1.02×10-4
approximate
(b)
T*1/2,B=infinity
0.025
0.02
0.015
0.01
0.005
0
r*ABP
0
0.01
0.02
0.03
0.04
0.05
0.06
t*
T*1/2,A=1.02×10-6
T*1/2,A=1.02×10-5
T*1/2,A=1.02×10-4
approximate

Figure 7

(a)

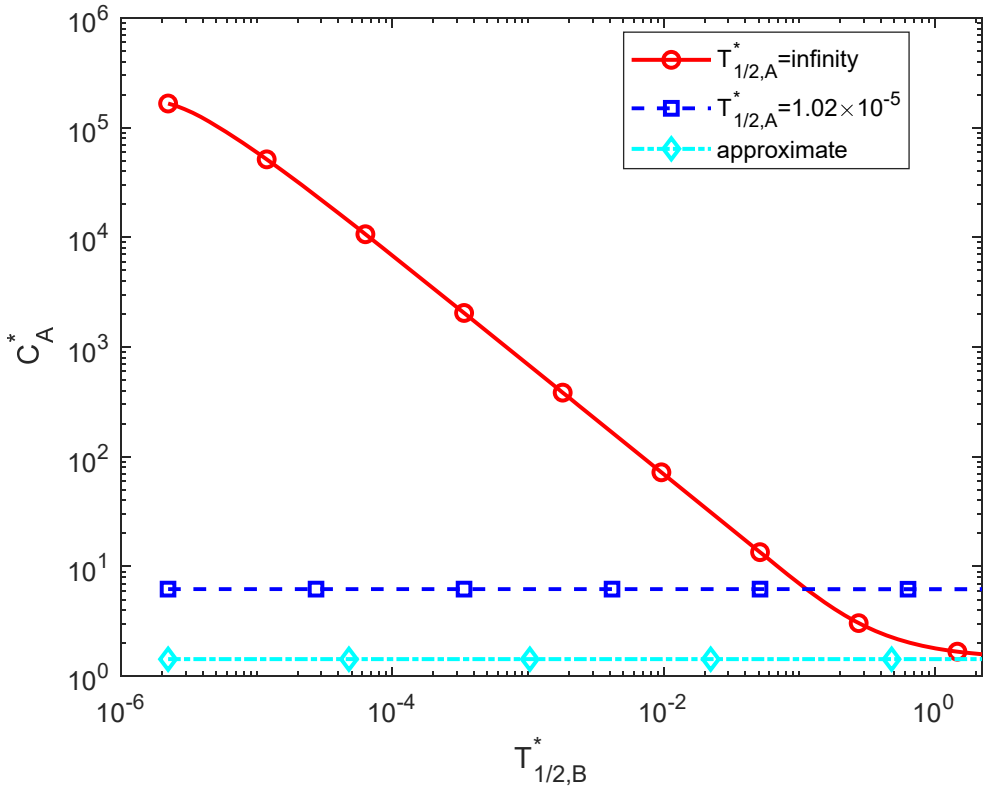
10^6
10^5
10^4
10^3
10^2
10^1
10^0
C^*_A
10^{-6}
10^{-4}
10^{-2}
10^0
$T^*_{1/2,B}$
$T^*_{1/2,A}$=infinity
$T^*_{1/2,A}=1.02\times10^{-5}$
approximate

(b)

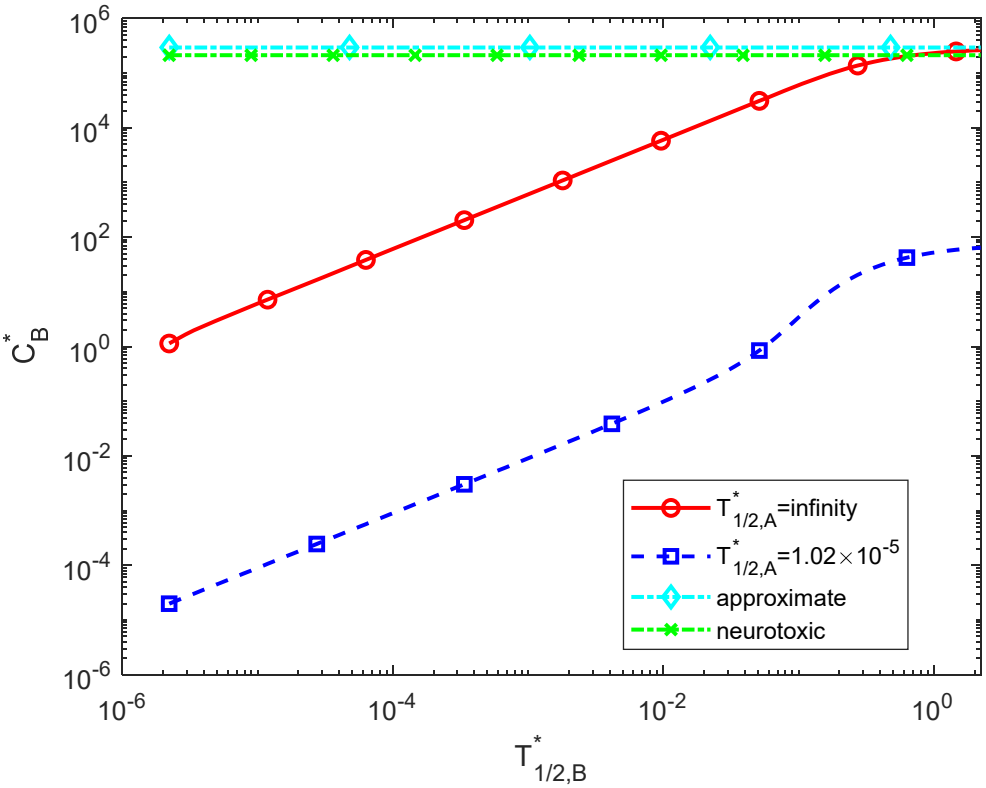
10^6
10^4
10^2
10^0
10^{-2}
10^{-4}
10^{-6}
C^*_B
10^{-6}
10^{-4}
10^{-2}
10^0
$T^*_{1/2,B}$
$T^*_{1/2,A}$=infinity
$T^*_{1/2,A}=1.02\times10^{-5}$
approximate
neurotoxic

Figure 8

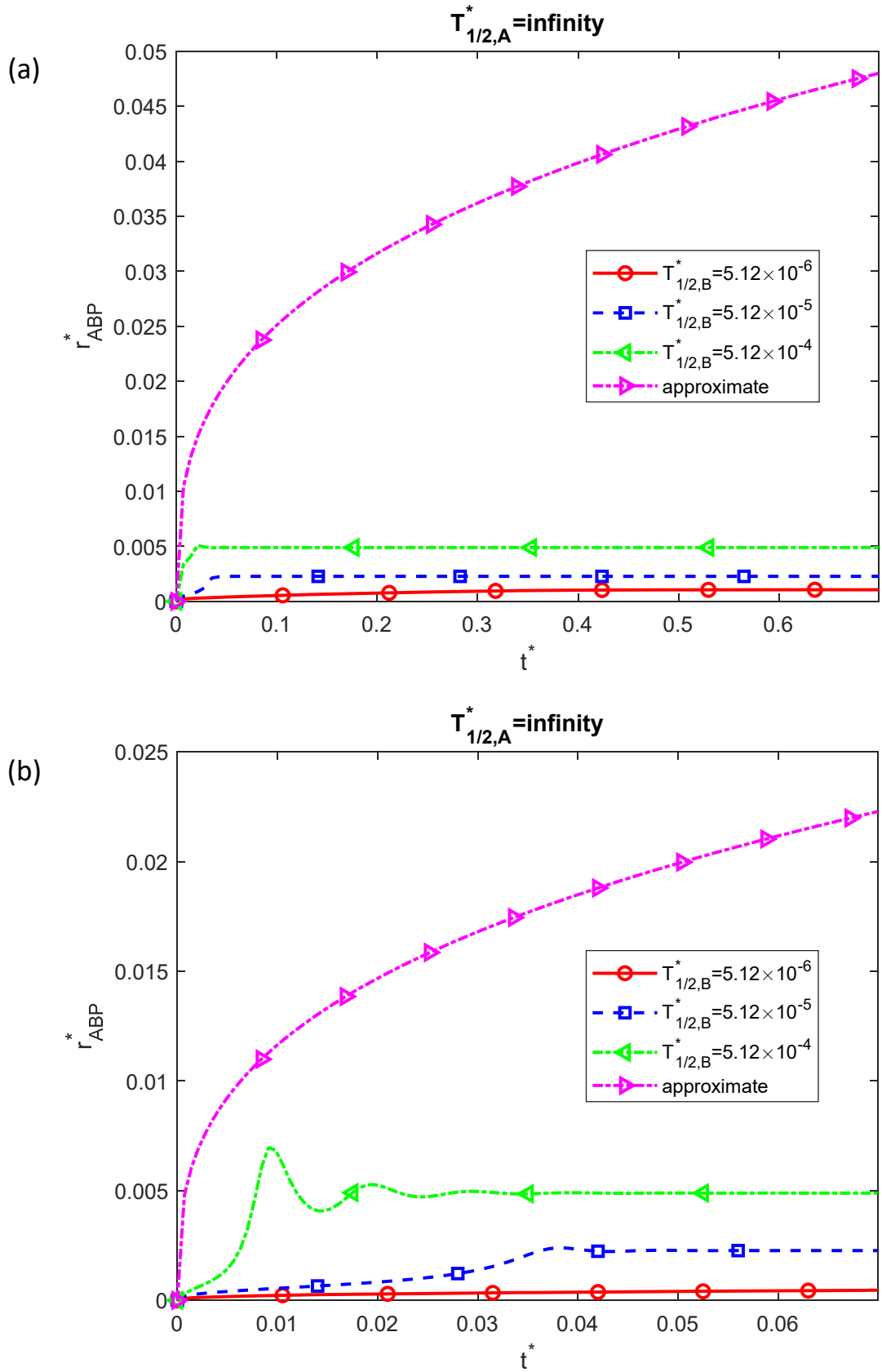
(a)
T*1/2,A=infinity
0.05
0.045
0.04
0.035
0.03
0.025
0.02
0.015
0.01
0.005
0
r*ABP
0
0.1
0.2
0.3
0.4
0.5
0.6
t*
T*1/2,B=5.12×10-6
T*1/2,B=5.12×10-5
T*1/2,B=5.12×10-4
approximate
(b)
T*1/2,A=infinity
0.025
0.02
0.015
0.01
0.005
0
r*ABP
0
0.01
0.02
0.03
0.04
0.05
0.06
t*
T*1/2,B=5.12×10-6
T*1/2,B=5.12×10-5
T*1/2,B=5.12×10-4
approximate

Figure 9

Numerical modeling of senile plaque development under conditions of limited diffusivity of amyloid-β monomers

Andrey V Kuznetsov

Department of Mechanical and Aerospace Engineering, North Carolina State University,

Raleigh, NC 27695-7910, USA; e-mail: avkuznet@ncsu.edu

Supplemental Materials

S1. Exact and approximate solutions of Eqs. (8)-(12) for the case of dysfunctional protein degradation machinery

The approximate and exact solutions for Eqs. (8)-(12) were derived in [21]. The procedure is summarized below.

If Aβ aggregation were diffusion-limited, aggregate growth would predominantly occur at the tips, resulting in a branching, tree-like structure. The absence of such structures implies that the process is not diffusion-limited [36].

For a large diffusivity of Aβ monomers, the CV can be treated as a lumped capacitance body, where concentrations depend solely on time, not on location. In this case, Eqs. (8)-(12) can be reformulated as the following system of ordinary differential equations:

$$\frac{dC_A^*}{dt^*} = -C_A^* - C_A^* C_B^* - C_A^* \frac{\ln(2)}{T_{1/2,A}^*} + q_{A,0}^* , \tag{S1}$$

$$\frac{\partial C_B^*}{\partial t^*} = C_A^* + C_A^* C_B^* - C_B^* \frac{\ln(2)}{T_{1/2,B}^*} , \tag{S2}$$

which must be solved subject to the following initial conditions:

$$\text{At } t^* = 0 : \; C_A^* = 0 , \; C_B^* = 0 . \tag{S3a,b}$$

The exact and approximate solutions are derived for the scenario when the protein degradation machinery is dysfunctional, implying infinitely large half-lives of Aβ monomers and aggregates, $T_{1/2,A}^* \to \infty$ and $T_{1/2,B}^* \to \infty$. When Eqs. (S1) and (S2) are added for this scenario, the following result is obtained:

$$\frac{dC_A^*}{dt^*} + \frac{dC_B^*}{dt^*} = q_{A,0}^* \,. \tag{S4}$$

By integrating Eq. (S4) and using the initial conditions given by Eq. (S3), the following result is obtained:

$$C_A^* + C_B^* = q_{A,0}^* t^* \,. \tag{S5}$$

The increase in $C_A^* + C_B^*$ over time is attributed to the continuous production of Aβ monomers. These monomers undergo continuous conversion into aggregates, and in the assumed scenario characterized by $T_{1/2,A}^* \to \infty$ and $T_{1/2,B}^* \to \infty$, neither monomers nor aggregates are subject to destruction.

The exact solution was derived using the following approach. C_A^* is eliminated from Eq. (S2) through the utilization of Eq. (S5):

$$\frac{dC_B^*}{dt^*} = q_{A,0}^* t^* - C_B^* + \left(q_{A,0}^* t^* - C_B^*\right) C_B^* \,. \tag{S6}$$

Eq. (S6) is similar to the one examined in [37]. To find the exact solution of Eq. (S6) with the initial condition given by Eq. (S3b), the DSolve function, followed by the FullSimplify function in Mathematica 13.3 (Wolfram Research, Champaign, IL), was utilized. The resulting solution is presented below:

$$C_B^*\left(t^*\right) = -1 + \frac{\exp\left(t^* + q_{A,0}^* \frac{\left(t^*\right)^2}{2}\right)\sqrt{q_{A,0}^*}}{\sqrt{q_{A,0}^*} - \sqrt{2} F\left(\frac{1}{\sqrt{2q_{A,0}^*}}\right) + \sqrt{2}\exp\left(t^* + q_{A,0}^* \frac{\left(t^*\right)^2}{2}\right) F\left(\frac{1 + q_{A,0}^* t^*}{\sqrt{2q_{A,0}^*}}\right)} \,. \tag{S7}$$

In this equation, $F\left(x\right)$ is Dawson's integral:

$$F\left(x\right) = \frac{1}{2}\sqrt{\pi}\, e^{-x^2} erfi\left(x\right), \tag{S8}$$

where $erfi\left(x\right)$ represents the imaginary error function.

If $t^* \to 0$, Eq. (S7) implies that

$$C_B^* \to \frac{q_{A,0}^* \left(t^*\right)^2}{2} \,. \tag{S9}$$

As the exact solution (S7) is hard to analyze for large t^* (due to the NaN error), an approximate solution valid for large values of t^* is derived. The analysis of numerical solutions in [21] indicates that as time increases, the concentration of Aβ aggregates linearly increases while the concentration of Aβ monomers decreases. Substituting this result into Eq. (S5) yields:

$$C_B^* = q_{A,0}^* t^* , \tag{S10}$$

which is valid for large t^*.

Substituting this into Eq. (S2), the following is obtained:

$$C_A^* = \frac{q_{A,0}^*}{1 + q_{A,0}^* t^*} . \tag{S11}$$

Eqs. (S10) and (S11) constitute the approximate solution for the concentrations of Aβ aggregates and monomers, respectively. Note that C_A^* given by Eq. (S11) violates the initial condition given by Eq. (5a) and hence is valid only for large t^*.

S2. Supplementary figures

(a)

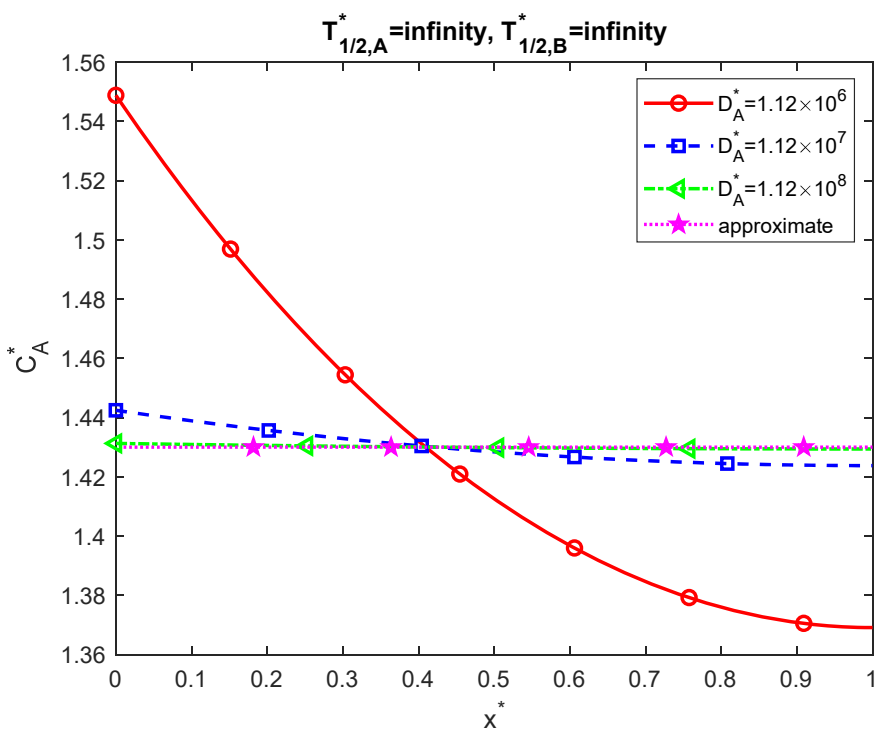

(b)

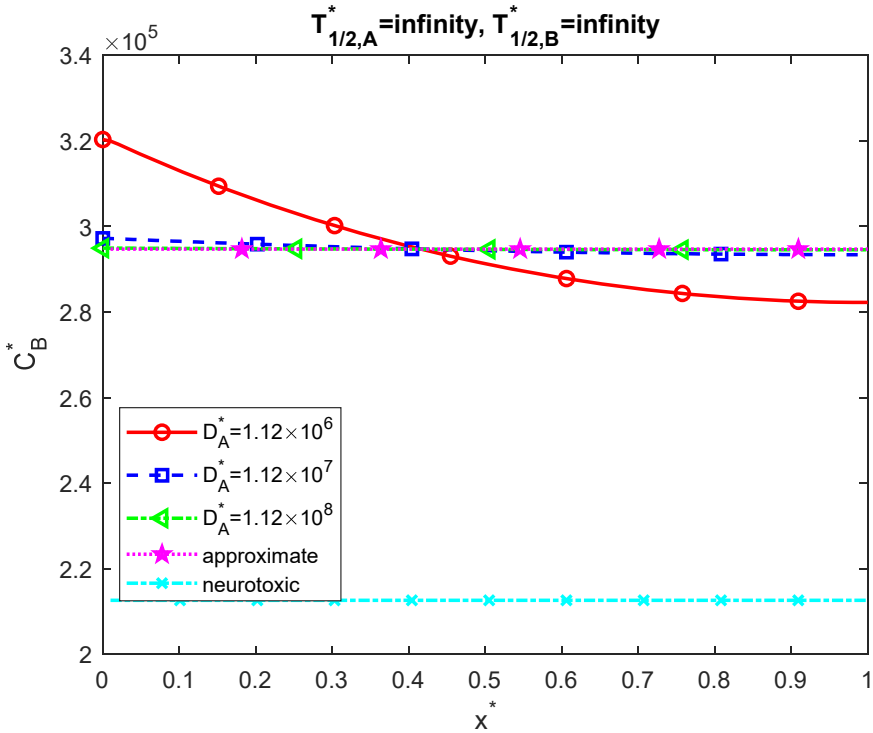

Fig. S1. Dimensionless molar concentrations of Aβ monomers, C_A^* (a) and Aβ aggregates, C_B^* (b) as a function of the dimensionless distance from the surface releasing Aβ monomers (e.g., cell membrane), x^*. Approximate solutions (independent of x^*) for C_A^* and C_B^* are computed using Eqs. (S11) and (S10), respectively. These results are presented at $t_f^* = 0.7$ (10 years) and correspond to the scenario with an infinite half-life of Aβ monomers and aggregates, $T_{1/2,A}^* \to \infty$ and $T_{1/2,B}^* \to \infty$, respectively. Results are shown for three values of the dimensionless diffusivity of Aβ monomers, D_A^*.

(a)

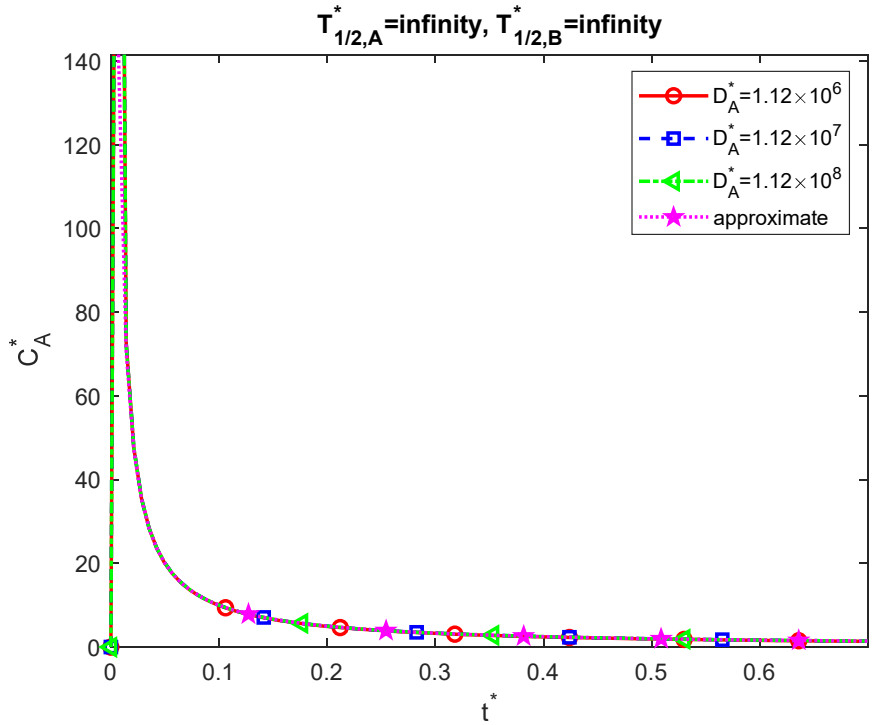
T*1/2,A=infinity, T*1/2,B=infinity
140
120
100
80
60
40
20
0
0
0.1
0.2
0.3
0.4
0.5
0.6
C*A
t*
D*A=1.12×10^6
D*A=1.12×10^7
D*A=1.12×10^8
approximate

(b)

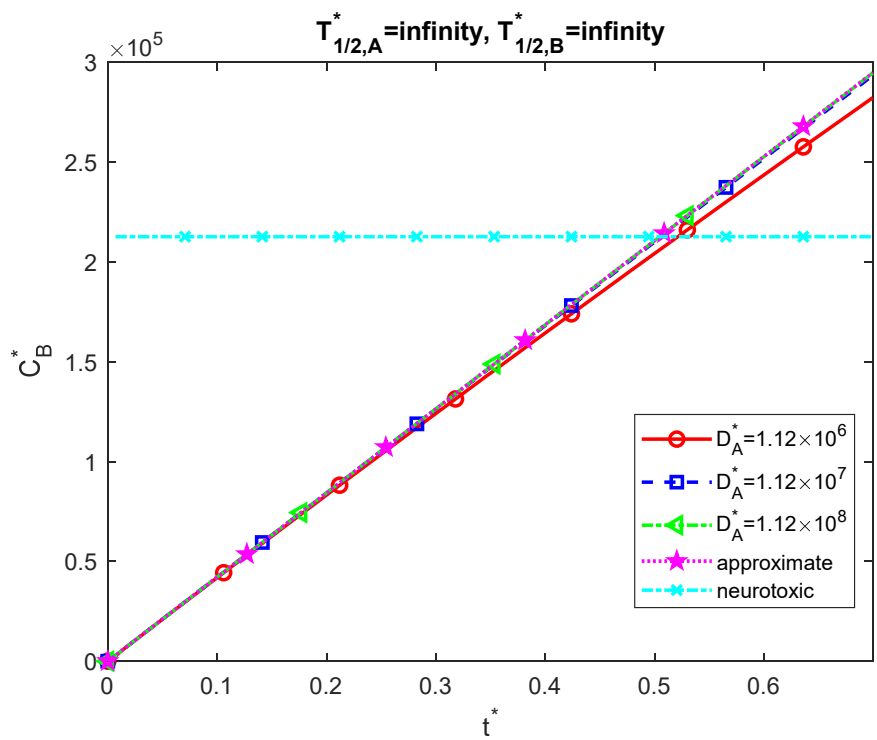
T*1/2,A=infinity, T*1/2,B=infinity
×10^5
3
2.5
2
1.5
1
0.5
0
0
0.1
0.2
0.3
0.4
0.5
0.6
C*B
t*
D*A=1.12×10^6
D*A=1.12×10^7
D*A=1.12×10^8
approximate
neurotoxic

Fig. S2. Dimensionless molar concentrations of Aβ monomers, C_A^* (a) and Aβ aggregates, C_B^* (b) as a function of dimensionless time, t^*. Approximate solutions for C_A^* and C_B^* are computed using Eqs. (S11) and (S10), respectively. The approximate solution for C_B^* is directly proportional to t^*. These results are presented at the right-hand side boundary of the CV, $x^*=1$, and correspond to the scenario with an infinite half-life of Aβ monomers and aggregates, $T_{1/2,A}^* \to \infty$ and $T_{1/2,B}^* \to \infty$, respectively. Results are shown for three values of the dimensionless diffusivity of Aβ monomers, D_A^*.

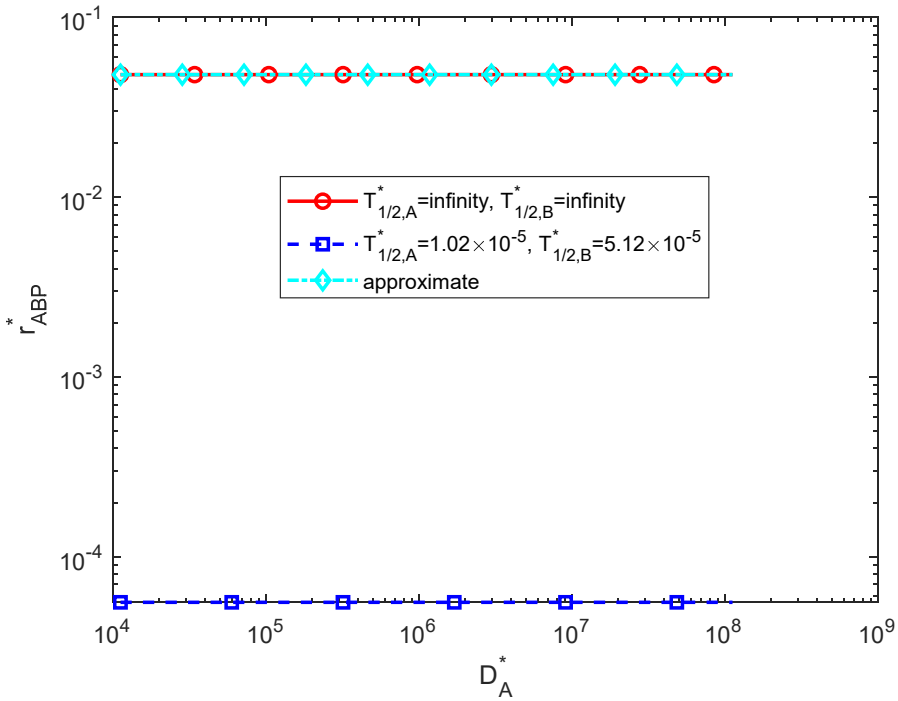

Fig. S3. Dimensionless radius of an Aβ growing plaque, r_{ABP}^*, as a function of the dimensionless diffusivity of Aβ monomers, D_A^*, at $t_f^*=0.7$ (10 years). Dimensional radius of Aβ plaque for infinite half-life of Aβ monomers and aggregates is 0.0480 (corresponding dimensional radius is 2.40 μm).

(a)

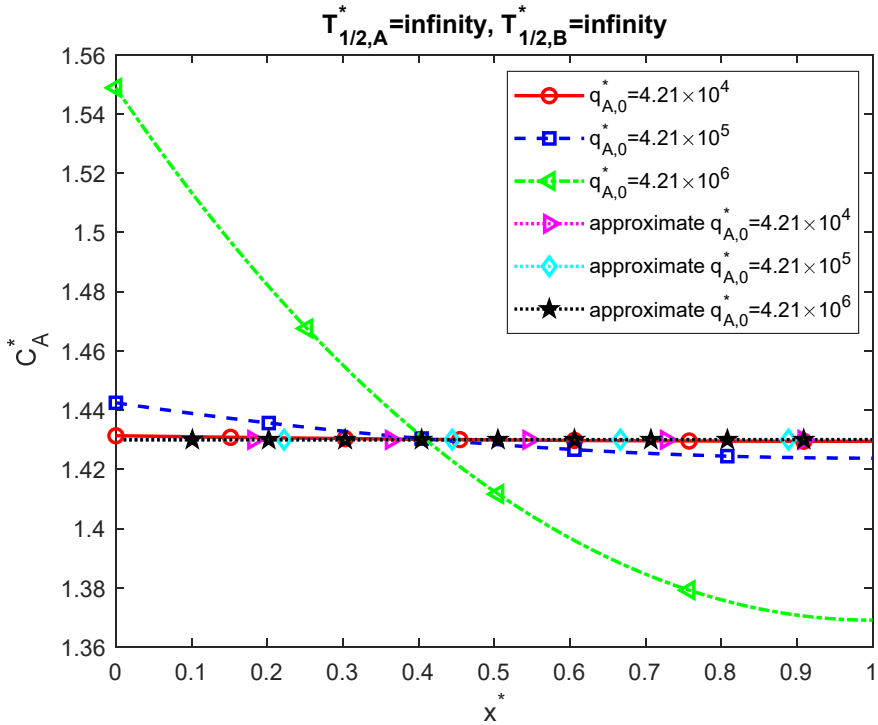
T*1/2,A=infinity, T*1/2,B=infinity
q*A,0=4.21×10^4
q*A,0=4.21×10^5
q*A,0=4.21×10^6
approximate q*A,0=4.21×10^4
approximate q*A,0=4.21×10^5
approximate q*A,0=4.21×10^6
C*A
x*

(b)

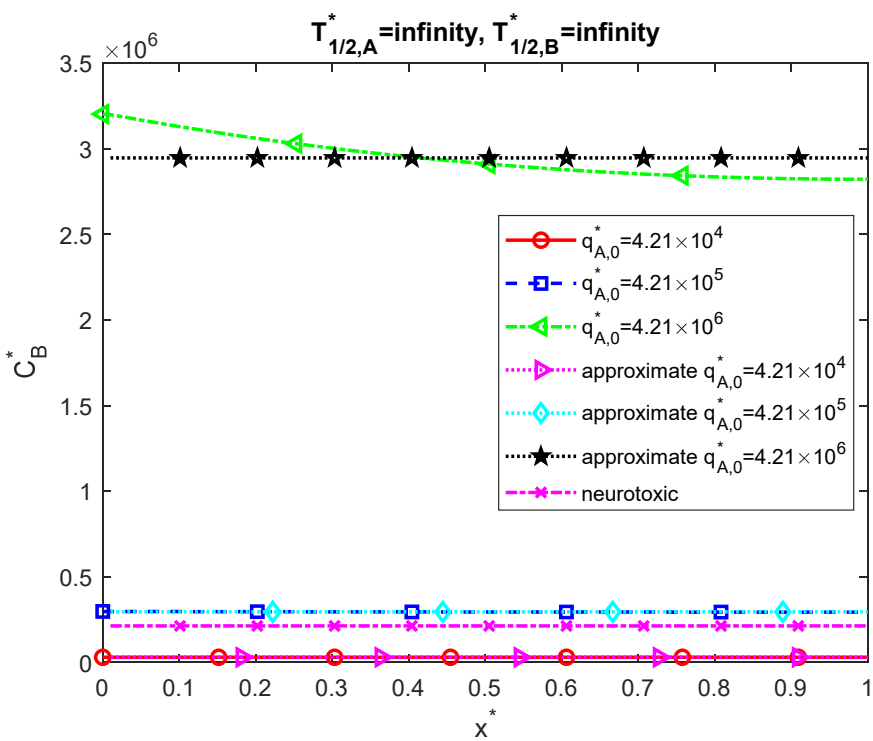
T*1/2,A=infinity, T*1/2,B=infinity
×10^6
q*A,0=4.21×10^4
q*A,0=4.21×10^5
q*A,0=4.21×10^6
approximate q*A,0=4.21×10^4
approximate q*A,0=4.21×10^5
approximate q*A,0=4.21×10^6
neurotoxic
C*B
x*

Fig. S4. Dimensionless molar concentrations of Aβ monomers, C_A^* (a) and Aβ aggregates, C_B^* (b) as a function of the dimensionless distance from the surface releasing Aβ monomers (e.g., cell membrane), x^*. Approximate solutions (independent of x^*) for C_A^* and C_B^* are computed using Eqs. (S11) and (S10), respectively. These results are presented at $t_f^* = 0.7$ (10 years) and correspond to the scenario with an infinite half-life of Aβ monomers and aggregates, $T_{1/2,A}^* \to \infty$ and $T_{1/2,B}^* \to \infty$, respectively. Results are shown for three values of the dimensionless flux of Aβ monomers from the left-hand side boundary of the CV, $q_{A,0}^*$.

(a)

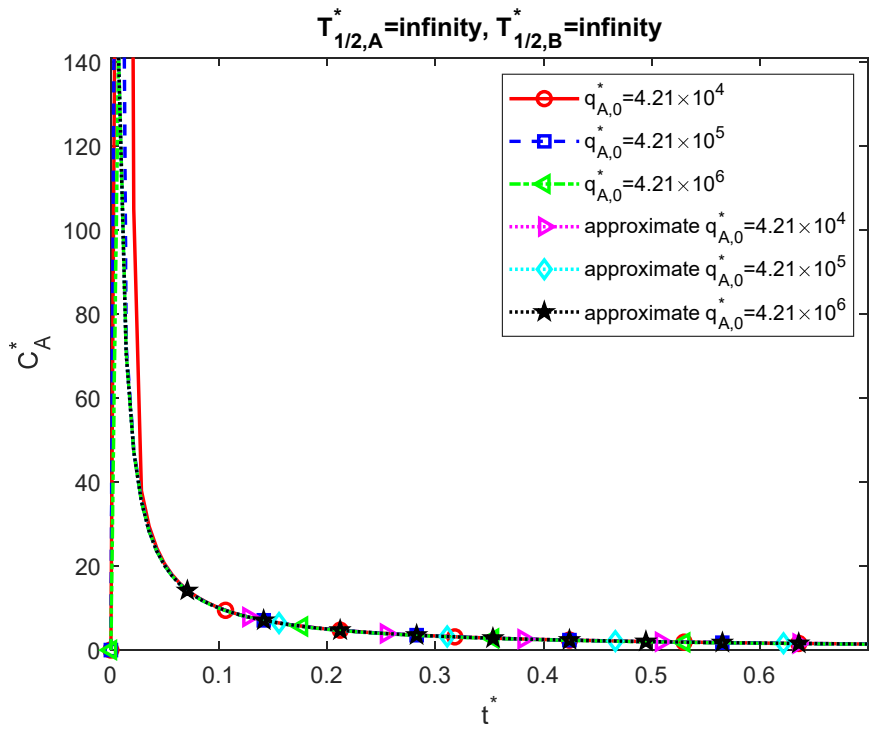

(b)

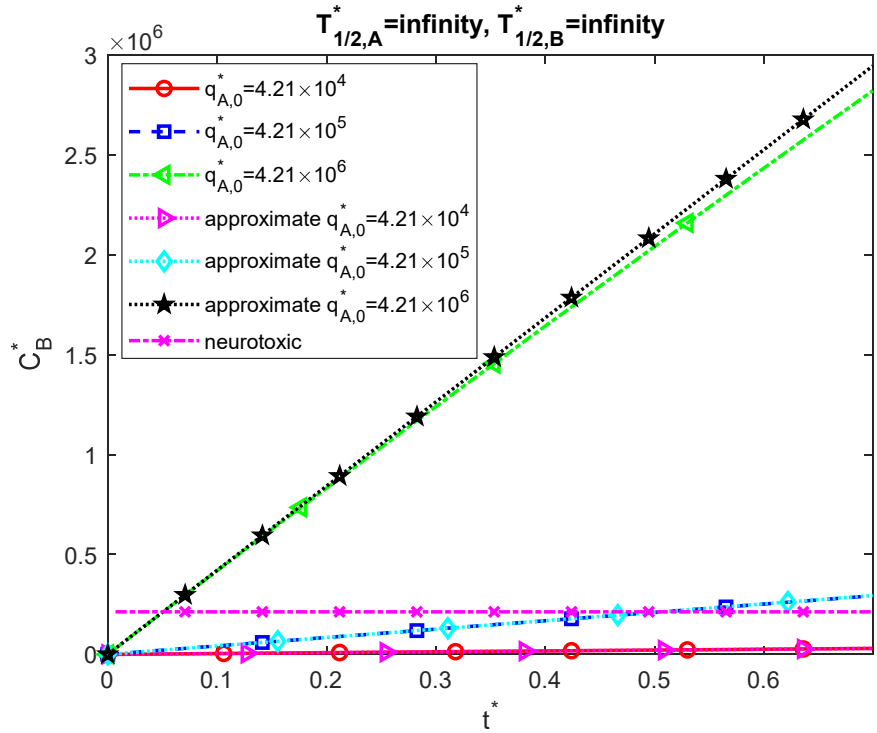

Fig. S5. Dimensionless molar concentrations of Aβ monomers, C_A^* (a) and Aβ aggregates, C_B^* (b) as a function of dimensionless time, t^*. Approximate solutions for C_A^* and C_B^* are computed using Eqs. (S11) and (S10), respectively. The approximate solution for C_B^* is directly proportional to t^*. These results are presented at the right-hand side boundary of the CV, $x^*=1$, and correspond to the scenario with an infinite half-life of Aβ monomers and aggregates, $T_{1/2,A}^* \to \infty$ and $T_{1/2,B}^* \to \infty$, respectively. Results are shown for three values of the dimensionless flux of Aβ monomers from the left-hand side boundary of the CV, $q_{A,0}^*$.

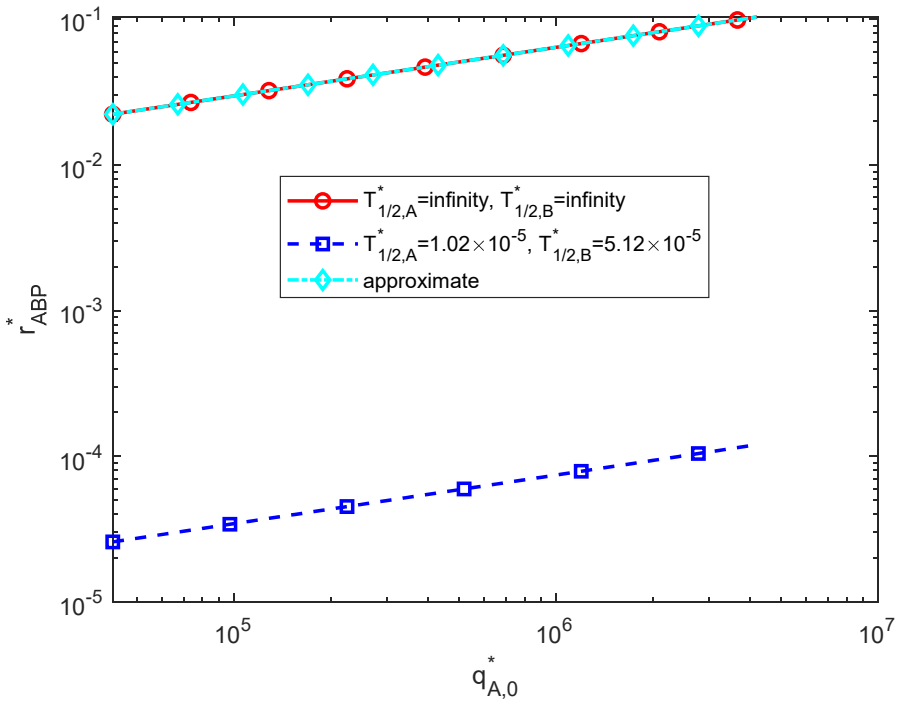

Fig. S6. Dimensionless radius of a growing Aβ plaque, r^*_{ABP}, as a function of the dimensionless flux of Aβ monomers from the left-hand side boundary of the CV, $q^*_{A,0}$, at $t^*_f = 0.7$ (10 years). Dimensionless radius of Aβ plaque corresponding to the largest value of $q^*_{A,0}$ in Fig. S6 is 0.103 (corresponding dimensional radius is 5.17 μm); this result is for the infinite half-life of Aβ monomers and aggregates.

(a)

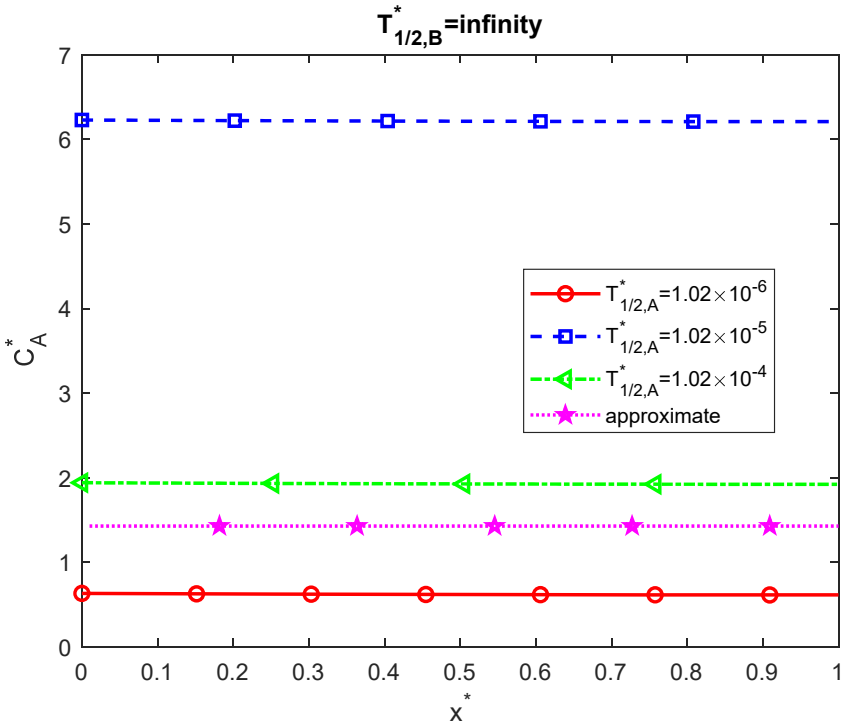
T*1/2,B=infinity
C*A
x*
T*1/2,A=1.02×10-6
T*1/2,A=1.02×10-5
T*1/2,A=1.02×10-4
approximate

(b)

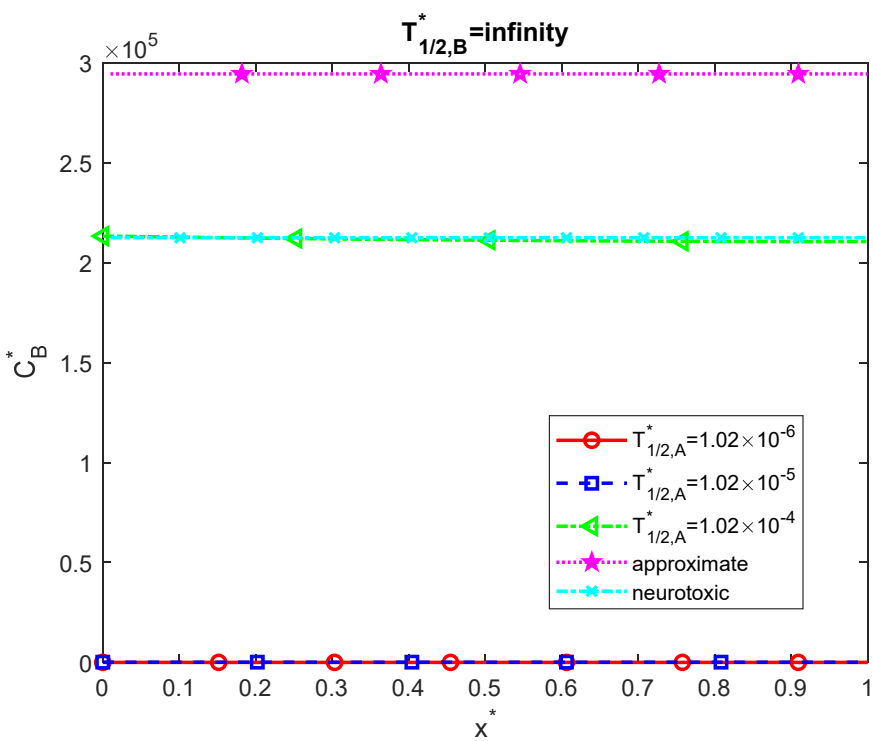
T*1/2,B=infinity
×10^5
C*B
x*
T*1/2,A=1.02×10-6
T*1/2,A=1.02×10-5
T*1/2,A=1.02×10-4
approximate
neurotoxic

Fig. S7. Dimensionless molar concentrations of Aβ monomers, C_A^* (a) and Aβ aggregates, C_B^* (b) as a function of the dimensionless distance from the surface releasing Aβ monomers (e.g., cell membrane), x^*. Approximate solutions (independent of x^*) for C_A^* and C_B^* are computed using Eqs. (S11) and (S10), respectively. These results are presented at $t_f^* = 0.7$ (10 years) and correspond to the scenario with an infinite half-life of Aβ aggregates, $T_{1/2,B}^* \to \infty$. Results are shown for three values of the dimensionless half-life of Aβ monomers, $T_{1/2,A}^*$.

(a)

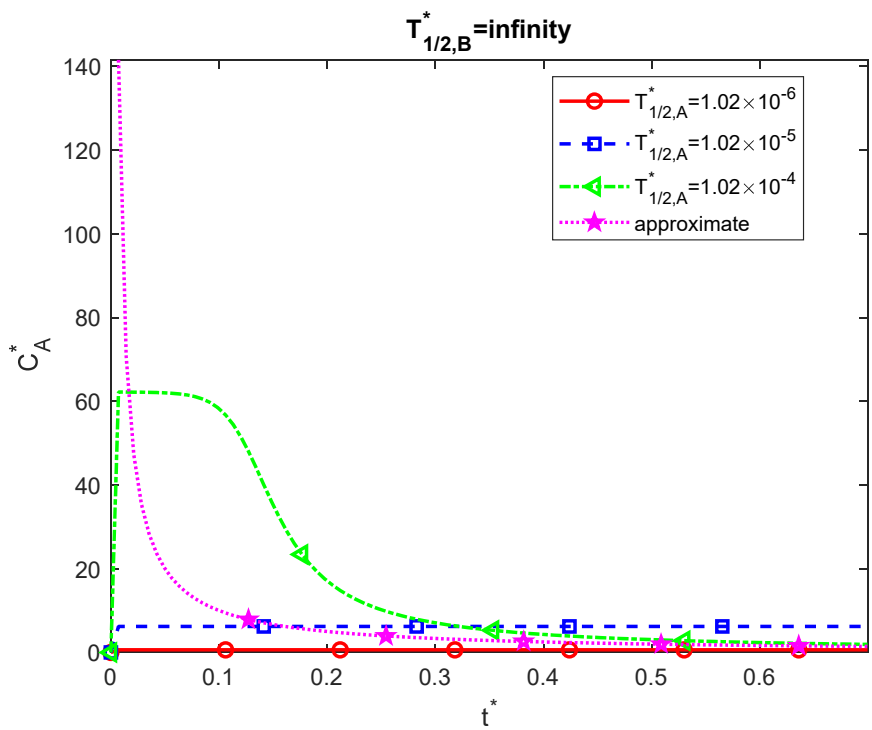

(b)

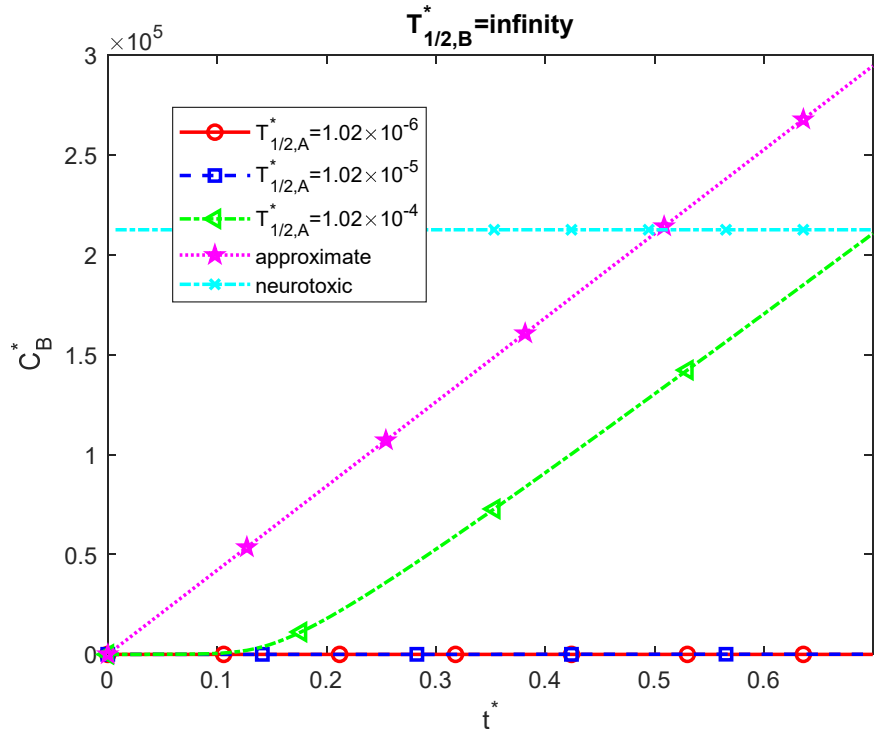

Fig. S8. Dimensionless molar concentrations of Aβ monomers, C_A^* (a) and Aβ aggregates, C_B^* (b) as a function of dimensionless time, t^*. Approximate solutions for C_A^* and C_B^* are computed using Eqs. (S11) and (S10), respectively. The approximate solution for C_B^* is directly proportional to t^*. These results are presented at the right-hand side boundary of the CV, $x^*=1$, and correspond to the scenario with an infinite half-life of Aβ aggregates, $T_{1/2,B}^* \to \infty$. Results are shown for three values of the dimensionless half-life of Aβ monomers, $T_{1/2,A}^*$.

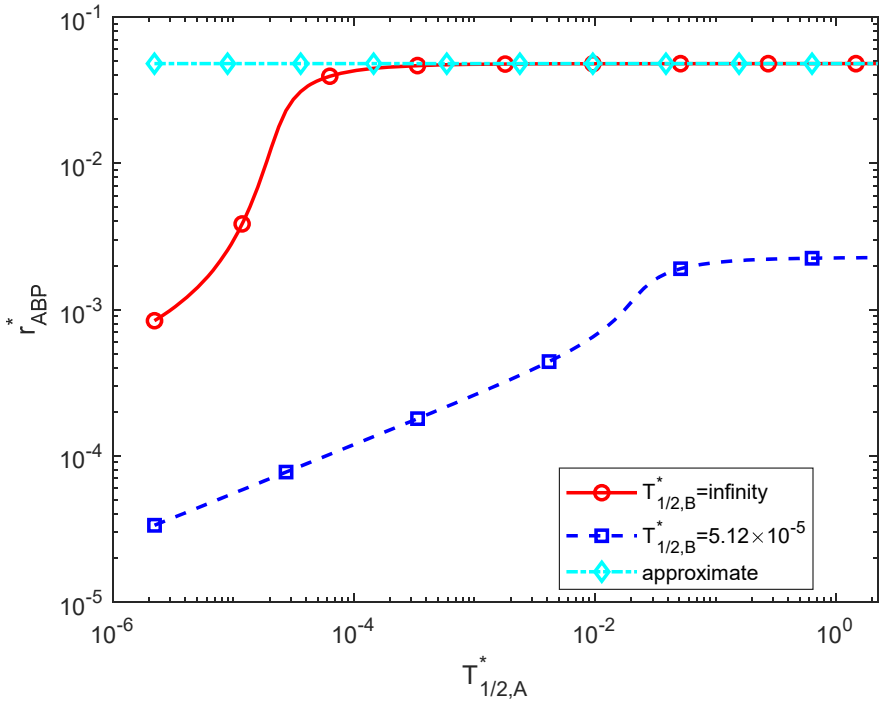

Fig. S9. Dimensionless radius of an Aβ plaque, r^*_{ABP}, as a function of the dimensionless half-life of Aβ monomers, $T^*_{1/2,A}$, at $t^*_f = 0.7$ (10 years). Dimensional radius of the Aβ plaque corresponding to the largest value of $T^*_{1/2,A}$ in Fig. S9 for infinite half-life of Aβ aggregates is 0.048 (corresponding dimensional radius is 2.40 μm).

(a)

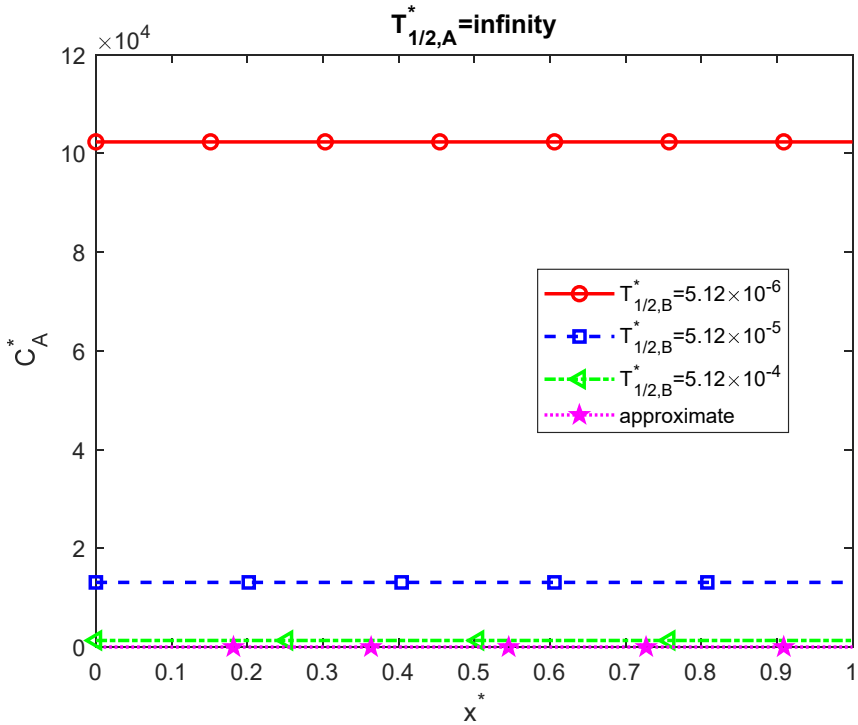
T*1/2,A=infinity
×10^4
12
10
8
6
4
2
0
C*A
0
0.1
0.2
0.3
0.4
0.5
0.6
0.7
0.8
0.9
1
x*
T*1/2,B=5.12×10^-6
T*1/2,B=5.12×10^-5
T*1/2,B=5.12×10^-4
approximate

(b)

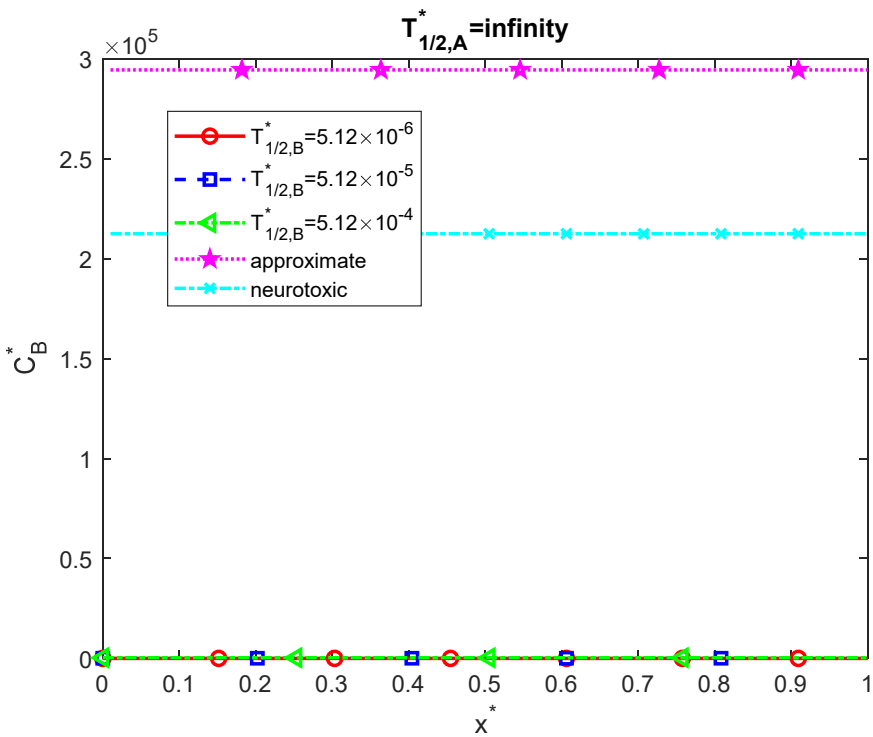
T*1/2,A=infinity
×10^5
3
2.5
2
1.5
1
0.5
0
C*B
0
0.1
0.2
0.3
0.4
0.5
0.6
0.7
0.8
0.9
1
x*
T*1/2,B=5.12×10^-6
T*1/2,B=5.12×10^-5
T*1/2,B=5.12×10^-4
approximate
neurotoxic

Fig. S10. Dimensionless molar concentrations of Aβ monomers, C_A^* (a) and Aβ aggregates, C_B^* (b) as a function of the dimensionless distance from the surface releasing Aβ monomers, x^*. Approximate solutions (independent of x^*) for C_A^* and C_B^* are computed using Eqs. (S11) and (S10), respectively. These results are presented at $t_f^* = 0.7$ (10 years) and correspond to the scenario with an infinite half-life of Aβ monomers, $T_{1/2,A}^* \to \infty$. Results are shown for three values of the dimensionless half-life of Aβ aggregates, $T_{1/2,B}^*$.

(a)

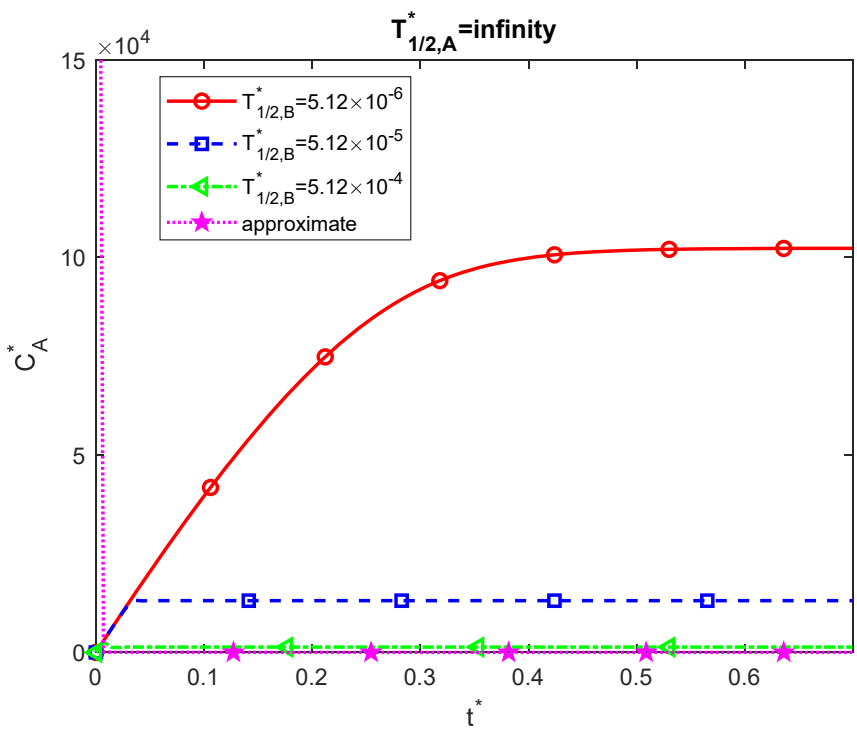

(b)

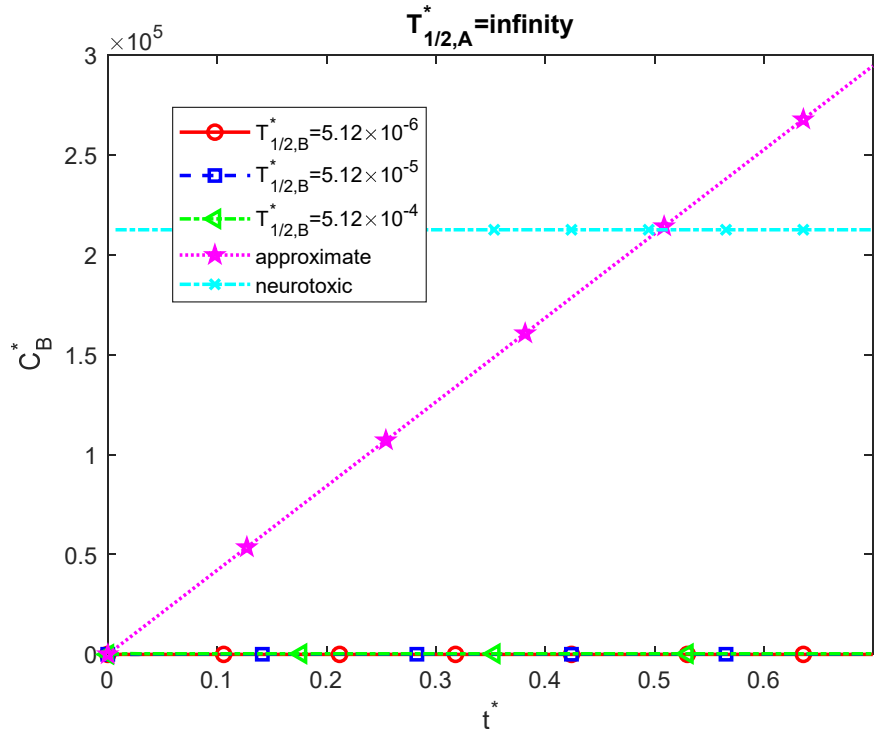

Fig. S11. The dimensionless molar concentrations of Aβ monomers, C_A^* (a) and Aβ aggregates, C_B^* (b) as a function of dimensionless time, t^*. The approximate solutions for C_A^* and C_B^* are determined using Eqs. (S11) and (S10), respectively. The approximate solution for C_B^* is directly proportional to t^*. These computational results are presented at the right-hand side boundary of the CV, $x^*=1$, depicting the scenario with an infinite half-life of Aβ monomers, $T_{1/2,A}^* \to \infty$. The results are presented for three different values of the dimensionless half-life of Aβ aggregates, $T_{1/2,B}^*$.

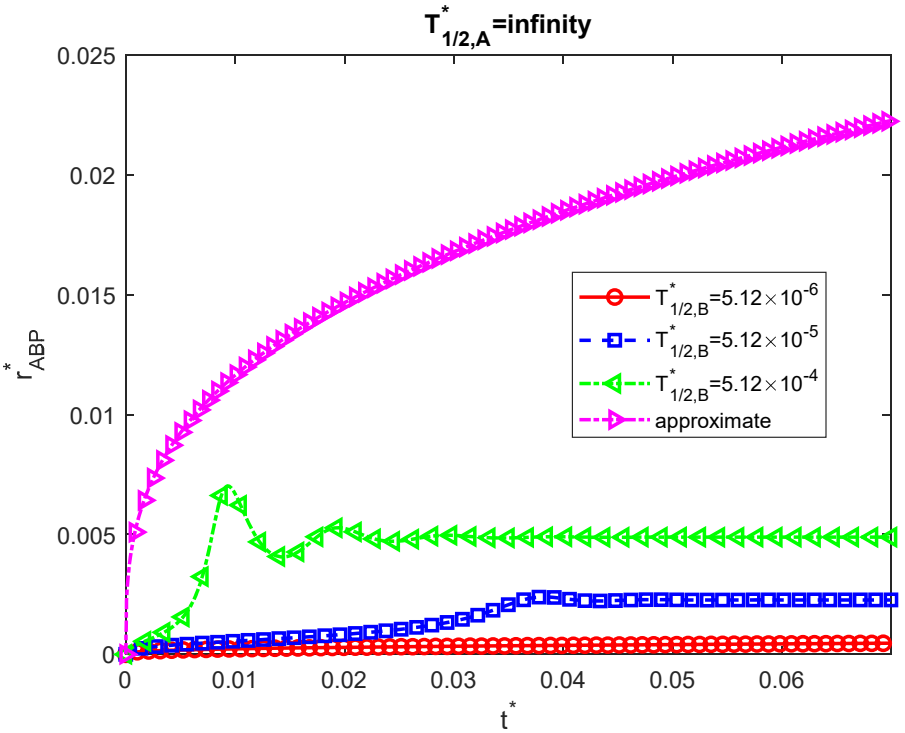

Fig. S12. Similar to Fig. 9b, this figure is computed with a mesh ten times finer with respect to t^* and x^* than Fig. 9b.

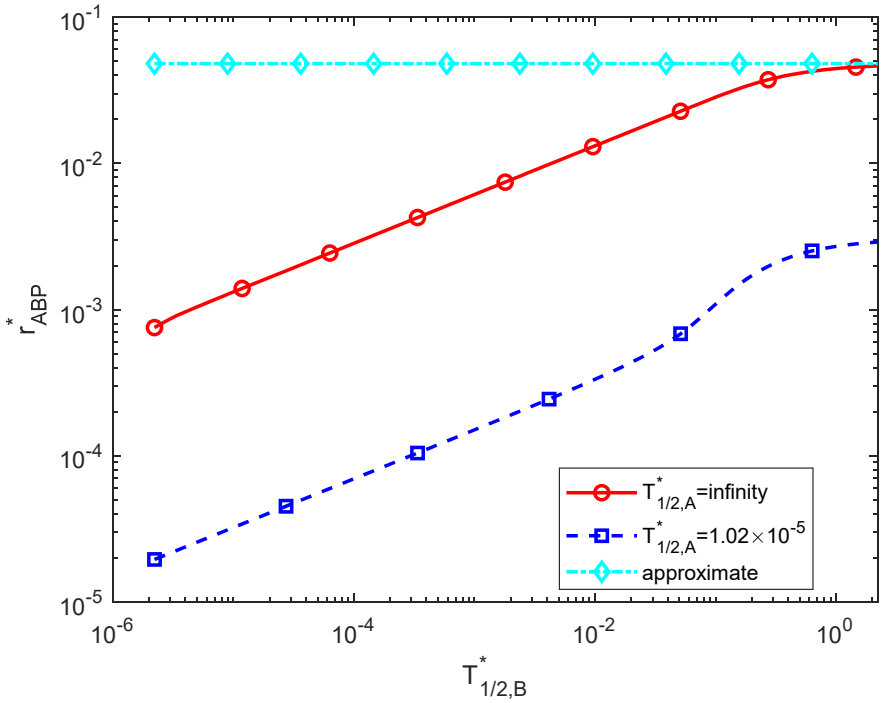

Fig. S13. The dimensionless radius of a growing Aβ plaque, r^*_{ABP}, as a function of the dimensionless half-life of Aβ aggregates, $T^*_{1/2,B}$, at $t^*_f = 0.7$ (10 years). The dimensionless radius of the Aβ plaque corresponding to the largest value of $T^*_{1/2,B}$ in Fig. S13 for the infinite half-life of Aβ aggregates is 0.046 (corresponding dimensional radius is 2.32 μm).